



Ionosphere response to three extreme events occurring near spring equinox in 2012, 2013 and 2015, observed by regional GNSS-TEC model

Anna Krypiak-Gregorczyk¹

Received: 30 March 2018 / Accepted: 2 November 2018 / Published online: 15 November 2018
© The Author(s) 2018

Abstract

Recent Solar Cycle 24 is characterized by the occurrence of three strong disturbances near an equinox. In this contribution, the responses of the ionosphere to the equinox storms in 2012, 2013 and 2015 driven by coronal mass ejections were analyzed. Due to the dynamic nature of changes in the ionosphere, the accuracy and resolution of existing global ionosphere models are often insufficient to reflect the storm-time effects in detail. Bearing this in mind, a new highly accurate and high-resolution regional ionosphere model was applied to study the response of this layer to severe geomagnetic storms over Europe. New regional total electron content (TEC) maps were derived exclusively from precise global navigation satellite systems (GNSS) carrier phase data. Although this study is based on space-geodetic technique, it was also carried out in relation to the observations provided from European ionosondes. In addition, the regional maps were compared to the final IGS Global Ionosphere Maps, where the new solution showed a better detail level. The results of storm-time temporal TEC changes provided by GNSS data were confirmed by NmF2 changes derived from ionosondes. Both data sources confirmed their high compatibility for studying the disturbed ionosphere. The magnetic storms that occurred on 7, 9, 12 and 15 March 2012 were different in nature. The largest change in the total electron content was observed during the storm of 9 March. This storm was associated with an interplanetary coronal mass ejection on 7 March that arrived on Earth 2 days later. The other analyzed events in 2013 and 2015 occurred on the same day of year—17 March. They were triggered by coronal mass ejections, which also hit the Earth magnetosphere at the same time of day. However, again the observed response of the ionosphere to these events was different.

Keywords Total electron content · Ionospheric electron density · GNSS · Ionosonde

1 Introduction

Investigations of ionosphere dynamics and disturbances during geomagnetic storms are still of high importance due to influence of the ionosphere on the space weather. The ionosphere, as an active layer, plays an important role in the space weather due to its sensitivity to the solar activity. In turn, the space weather affects satellite systems, energy transport, air traffic and, in consequence, the economy (Schrijver et al. 2015). Therefore, the studies of the ionosphere behavior play a very important role in understanding and forecasting of the space weather. The ionosphere is a layer of the atmosphere consisting mostly of ionized particles, which causes the satel-

lite electromagnetic signals to be delayed, fluctuations in signal strength and other adverse effects. The magnitude of these ionospheric effects largely depends on the state of the varying ionosphere, its total electron content (TEC) and the frequency of electromagnetic waves. The dynamic changes of the ionosphere are most easily divided into regular and sudden ones. Regular changes are directly related to the periodicity of the factors influencing them, such as the solar cycle lasting 11 years or seasonal variations. These regular variations are somewhat easy to model (Bilitza and Reinisch 2008; Maruyama et al. 2009).

Events such as coronal mass ejections could induce a series of disturbances in the ionosphere driven by a magnetic storm. This results in sudden disturbances in the ionosphere. This phenomenon is often called an “ionospheric storm.” The behavior of ionospheric storms can be different, as the storms can be characterized by positive or negative changes in the electron density. Generally, ionospheric storms are a global

✉ Anna Krypiak-Gregorczyk
krypiakanna@wp.pl

¹ Institute of Geodesy, University of Warmia and Mazury in Olsztyn, Oczapowskiego 2, Olsztyn, Poland

phenomenon. They happen because, due to a magnetic storm, the density of electrons increases, leading to the creation of regions of storm-enhanced plasma density (SED). This phenomenon is closely related to daytime positive disturbances and manifests several or even a 20-fold increase in the electron density in comparison with the normal sunset conditions. Therefore, permanent monitoring of the ionospheric state is required to mitigate the possible effects this may have on navigation and communication systems and other space and ground infrastructure (Maruyama et al. 2009).

All geomagnetic storms are characterized by an intensification of the ring current, usually resulting in a decrease in the geomagnetic activity Dst index below a set threshold. Furthermore, prolonged periods of southward interplanetary magnetic field (IMF) play a major role in the generation of geomagnetic storms. According to Wu et al. (2016a), a large southward IMF can be associated with an interplanetary shock wave (sheath) (Wu and Lepping 2016), a magnetic cloud (MC) or an interplanetary coronal mass ejection (ICME) (Wu and Lepping 2011) or a combination of these interplanetary structures.

As it was presented by Belehaki et al. (2017), the correlation between southward interplanetary magnetic field and the Earth's magnetic field leads to a strong electric field during the day. It can cause significant changes in the Earth's ionosphere, which are especially pronounced at low latitudes. However, as pointed out by Tsurutani et al. (2004), plasma enhancements are often observed during intense storm-time eastward electric fields. Then, the range of this plasma reaches middle latitudes. This phenomenon is called "superfountain effect." The increases of dayside TEC at these latitudes can amount to up to 80% compared to a quiet day.

In recent decades, the electron density perturbations are often monitored based on the analysis of observations from satellite navigation systems, which have become kind of ionosphere scanners, and are excellent supplements of classical sounding methods. For over 20 years, space-geodetic techniques such as global navigation satellite systems (GNSS) data from ground permanent networks governed by International GNSS Service (IGS) and EUREF Permanent Network (EPN) have allowed to determine the ionospheric TEC in regional and global scales (Afraimovich et al. 1998; Hernandez-Pajares et al. 2006; Tsurutani et al. 2004). Earlier, the ionosondes were principal source of the ionosphere sounding, providing valuable information about the analytic function of electron density with height, and also the propagation of perturbations at different altitudes (Hajkowicz 1992). However, these facilities have limitations arising from their number and information delivery which has reference only to the conditions in the lower part of ionosphere over limited areas. In recent years, we can observe examples of TEC modeling with the additional use of terrestrial ionosondes, and the obtained results pro-

vide an excellent, reliable source of information, supporting the satellite systems in the ionosphere modeling (Belehaki et al. 2012, 2015). Nevertheless, most of the observation-based ionosphere models are still based on the observations from GNSS. Most of them are developed using carrier phase-smoothed pseudorange data, which is characterized by low accuracy and requires strong smoothing of the results (Ciraolo et al. 2007). The recent analyses of these models evaluate their absolute accuracy at the level of 4–8 TEC units (TECU) and relative accuracy at only 20–30% (Hernandez-Pajares et al. 2017). Therefore, these models can be useful to the general overview of the ionosphere response to a geomagnetic storm. However, due to the dynamic nature of changes in the ionosphere, not only during geomagnetic storms, the resolution of existing models is often insufficient to analyze the storm-time effects in detail (Astafyeva et al. 2015). Therefore, in order to have more detailed information about the ionospheric changes over the selected area, especially in the studies of disturbed conditions, it is necessary to use more accurate ionosphere maps based on improved ionosphere modeling techniques, which are also derived with higher temporal and spatial resolution. For this reason, two major approaches to detailed ionospheric TEC estimation based on carrier phase data were developed. The first one applies precise point positioning technique, where carrier phase ambiguities and interfrequency biases are estimated in the geometry-based positioning model (Ren et al. 2016; Liu et al. 2018; Nie et al. 2018). The second one is based on a direct carrier phase bias estimation using geometry-free model, and this approach is applied in this research (see Sect. 3.1).

This paper describes our studies on the response of the ionosphere layer to the largest geomagnetic storms during Solar Cycle 24. Three extreme events having immense importance to space weather were discussed. For analyses, we applied the new highly accurate and high-resolution regional ionospheric TEC model based on multi-GNSS carrier phase data. Our European TEC maps are characterized by 2-min time interval and 0.2° spacing in both latitude and longitude. The accuracy of the vertical TEC maps is assumed to be better than 1 TECU (Krypiak-Gregorczyk et al. 2017b). In addition, critical frequency foF2 data from two ground-based ionosondes located in Europe was used for comparisons with GNSS estimates.

2 Overview of major disturbances of the Solar Cycle 24

The current Sunspot Cycle 24 is the lowest one since Cycle 14, in which the maximum smoothed sunspot number occurred in February 1906. The Sunspot Cycle 24 has two peaks: the first reached the smoothed sunspot number maximum in March 2012 and the second peak, which reached

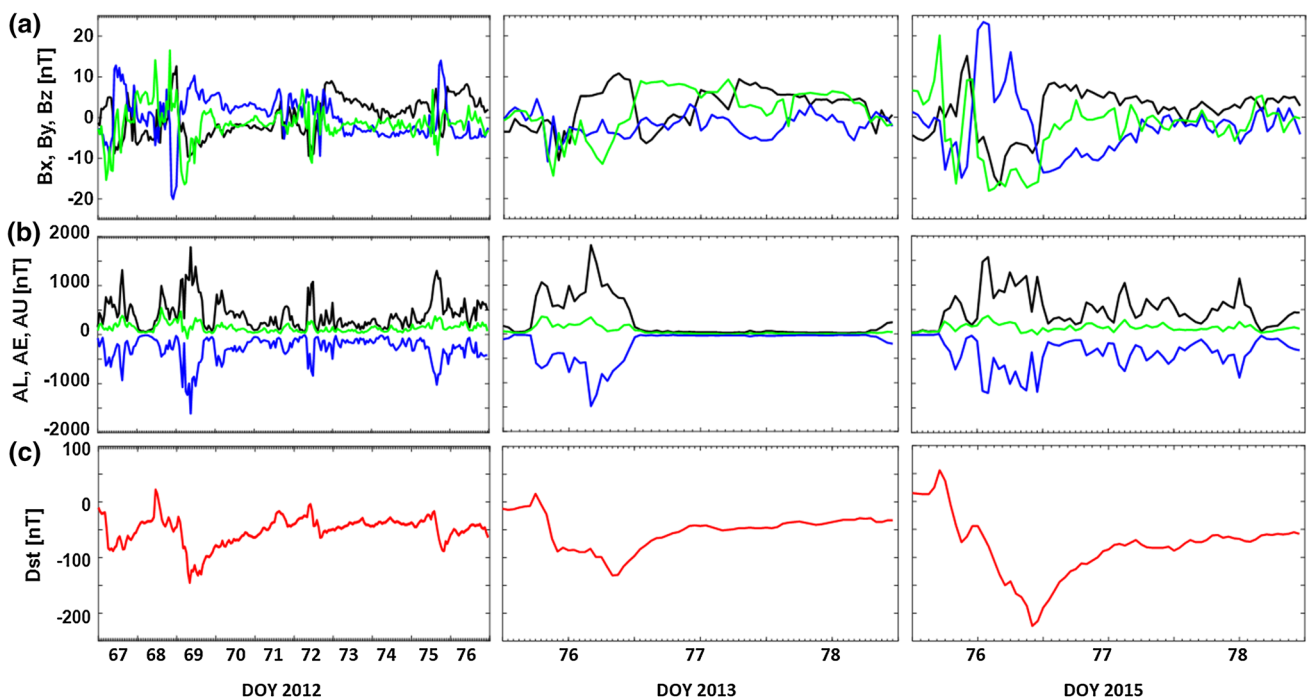


Fig. 1 Variability of interplanetary (IMF Bx, By, Bz), ionospheric (AL, AE, AU) and magnetospheric (Dst) parameters during intense geomagnetic storms of 7–16 March 2012 (DOY 67–76), 17–19 March (DOY

76–78) 2013 and 2015. **a** the interplanetary magnetic field parameters (IMF Bx-black, By-blue and Bz component-green), **b** the auroral electrojet indexes (AL-black, AE-blue and AU-green), **c** Dst index (red)

the highest number of sunspots, took place in April 2014 and was larger than the first one. In this paper, three very strong geomagnetic storms that took place near the spring equinox were selected for a study on regional ionosphere response to the geomagnetic storm.

It is well known that the geomagnetic storms take place as a result of the transfer of solar energy into the magnetosphere following magnetic reconnection between the southward IMF Bz component and the antiparallel geomagnetic field at the magnetopause (Dungey 1963; Gonzalez et al. 1994; Okpala and Ogbonna 2017). An interplanetary CME reaching to Earth with a preceding shock usually leads to classic three steps of geomagnetic storm phase: a sudden commencement generated by the shock, the main phase and then a recovery phase. The studies conducted by many authors have shown that 95% of strong geomagnetic storms were associated with coronal mass ejection (Tripathi and Mishra, 2006; Liu et al. 2015). Moreover, Gonzalez and Tsurutani (1987) indicated that two structures: interplanetary field strength and directional components (mainly negative Bz) are essential for the development of the storm.

2.1 Storms taking place in 2012, 2013 and 2015

The first major geomagnetically active period of the ascending phase of the Solar Cycle 24 took place from 7 to 16 March 2012. An extensive overview of major solar, interplanetary,

magnetospheric, and ionospheric features and causes of this active period was provided by Tsurutani et al. (2014) and Belehaki et al. (2017). Figure 1 gives an overview of the interplanetary data for the analyzed period for the three space weather events. Starting from the top the panels present: interplanetary magnetic field parameters (Bx, By, Bz), the auroral electrojet indexes (AL, AE, AU) and the disturbance storm-time index (Dst), which are used to identify the occurrence and intensity of magnetic storms.

According to the universal definition of the storm as used in practice, when the intensities reach $Dst < -50$ nT, it signifies the occurrence of a magnetic storm. Thus using this definition, during the first of the analyzed periods four storms were identified: on 7, 9, 12 and 15 March with the peaks intensity of Dst: -98 nT, -148 nT, -67 nT, -79 nT, respectively. The first magnetic storm on 7 March (DOY 67) was initiated by southward directed interplanetary sheath fields IMF Bz observed before the first interplanetary shock, which occurred at 03:28 UT on 7 March. The main phase of the magnetic storm began when solar wind energy was transferred to the magnetosphere due to the magnetic reconnection between the southwardly sheath fields and the northwardly magnetopause fields, as pointed out by Tsurutani et al. (2014). This phase started at $\sim 2:00$ UT on 7 March and reached the maximum at $\sim 5:15$ UT. The Dst peak intensity was -98 nT. The intense southward IMF component amounted to ~ 17 nT in the sheath behind the shock and

correlated well with the Dst decrease, but with a slight delay. According to Belehaki et al. (2017), the magnetic storm initiated on 8 March (DOY 68) was characterized by a different nature and a different interplanetary cause. At 11:30 UT on 8 March, as a result of shock compression of the magnetosphere, an intense sudden impulse occurred (Joselyn and Tsurutani 1990; Araki et al. 2009; Belehaki et al. 2017). As it can be seen in Fig. 1, AU index reflecting the directly driven component of auroral activity and AL index containing significant contributions from directly driven and substorm expansion phase activity, increased almost symmetrically. The reading of the AU index achieved slightly higher values than the AL index. During the whole directly driven phase, the IMF Bz parameter reached positive values, and after the intense sudden impulse, all IMF components presented strong pulsations. On the next day, the IMF Bz returned to the south, the AL index fell suddenly and the AU index stayed at very low values. Due to the magnetic reconnection between the southwardly sheath fields and the northwardly magnetopause fields, the solar wind energy was transferred to the magnetosphere. Thus, the loading–unloading mechanism in the magnetosphere was fully developed (Tsurutani et al. 2014). The main phase of the storm began and reached a peak intensity of $Dst = -131$ nT at 8:00 UT on 9 March (DOY 69). The next event on 12 March (DOY 72) was a “double-shock” event: the first one at ~12:28 UT on 11 March and a second one at ~08:30 UT on 12 March. In the first case, the values of magnetic field doubled across the shock. The second shock on 12 March exhibited an enhanced magnetic field. The cause of this magnetic storm was the southward component of the high-intensity magnetic field. The shock occurring on this day triggered a “supersubstorm.” The AE index was above 1500 nT. The last storm during this period took place on March 15 (DOY 75) and was characterized by the Dst index peaking at around 20:00 UT. The interplanetary shock occurred at ~23:3 UT. Then, the IMF Bz amounted to ~−5 nT, and the Dst index did not exceed −30 nT.

The first super geomagnetic storm of Solar Cycle 24 occurred on 17 March 2015 (DOY 76) and was called the St. Patrick’s storm. It should be emphasized that it was a two-step storm. Namely, the solar event on 15 March 2015 can be considered the initial cause of the storm. The storm intensified with the arrival of a coronal mass ejection (CME) at 04:45 UT (Wu et al. 2016a). The interplanetary magnetic field (IMF) turned northward. The Bz component increased from +10 to +26 nT, and an increase in the Dst index amounted from +10 to +60 nT (Fig. 1). At the same time, the AE magnetic index reached a small peak of 300 nT. The Bz component turned southward at around 06:00 UT, reaching the value of −22 nT at 06:20 UT. At this time, the compression phase had ended. The AE magnetic index grew reaching the maximum value of 1016 nT around 09:30 UT, and the Dst index decreased and reached the minimum value of −97 nT at

around 10:00 UT. From ~09:30 UT until 12:00 UT, there was a partial recovery phase. The Bz was again northward, the AE index decreased to ~50 nT and the Dst increased from −97 to −38 nT. Then a large MC field caused the second storm intensification. The main phase of this storm began when the IMF Bz started turning southward after 12:00 UT, and Dst index began gradually decreasing. At around 13:00 UT, the Bz component changed direction for a very short period, and at this time the AE index reached the maximum value of 2298 nT. Then the Bz became southward again and remained southward until 24:00 UT. During this main phase of the storm that lasted 18 h, the Dst kept falling, reaching the minimum value ($Dst = -223$ nT) at 22:45 UT. During the recovery phase, the Dst was increasing to −50 nT and the magnetic index AE exhibited a few peaks larger than 800 nT (Liu et al. 2015; Singh et al. 2015).

The last of the analyzed storms was the one of 17 March 2013 (DOY 76). This event, like the previous one, took place on St. Patrick’s Day. This storm was triggered by a coronal mass ejection that occurred on 15 March (Wu et al. 2016b). The changes in IMF parameters (Bx, By and Bz) indicate the shock arrival at 06:00 UT on 17 March, which caused the sudden commencement (SC) of the storm. With the beginning of the storm, there was a sudden drop in the Dst values. The double-phase minimum $Dst \sim -107$ nT at around 10:30 UT and 12:00 UT was observed. The first southward turning of Bz occurred almost immediately after the shock arrival at ~06:00 UT and stayed southward throughout the main phase of the storm. However, at this time (06:00–24:00 UT), there were fluctuations with several northward turnings. During the storm, the By component changed amplitude from −10 to 10 nT, while an immediate onset of intense auroral activity is seen in the AE index. At about 15:30 UT on 17 March, a MC occurred indicated by intense magnetic fields with a general lack of Alfvén waves and discontinuities (Tsurutani et al. 1988; Verkhoglyadova et al. 2016). Then, the IMF Bz turned southward in the MC. The Dst index noted the second decrease, reaching −132 nT at around 20:30 UT on 17 March, creating the second main phase storm (Fig. 1).

2.2 Data and methods used

An analysis of the ionosphere response to the selected geomagnetic storms was carried out based on a new regional ionospheric model developed at the Institute of Geodesy of the University of Warmia and Mazury in Olsztyn (UWM). The new model is based on precise un-differenced dual-frequency GPS+GLONASS carrier phase data. This approach is based on a single-layer ionosphere approximation and uses a three-step procedure. Firstly, a carrier phase bias B_{iGF}^k of geometry-free linear combination is estimated

with the use of least squares approach. The observation equation is:

$$L_{iGF}^k = -\xi_{GF}\Delta I_i^k + B_{iGF}^k \quad (1)$$

with

$$B_{iGF}^k = \lambda_1 N_{i1}^k - \lambda_2 N_{i2}^k - (b_{L1}^k - b_{L2}^k) - (b_{L1,i} - b_{L2,i}) \quad (2)$$

where L_{iGF}^k is geometry-free combination of dual-frequency carrier phase signals transmitted by satellite k and received by receiver i , ΔI_i^k is ionospheric delay, B_{iGF}^k is carrier phase bias and ξ_{GF} is a factor relating the ionospheric delay to LI signal. Note that the carrier phase bias consists of differences between the carrier phase ambiguities N_{i1}^k and N_{i2}^k , and also receiver and satellite hardware delays b (interfrequency bias) (Eq. 2). Here, the unknown parameters are coefficients of the function parameterized for the ionosphere and carrier phase bias B_{iGF}^k for each continuous observational arc. The ionosphere is parameterized every 10 min using spherical harmonics expansion. The resulting coefficients are treated as nuisance parameters. However, the estimated bias is used in the second step to calculate precise ionospheric delays ΔI_i^k (Eq. 2). This can be done for every observational epoch, e.g., at 30 s. Then, the ionospheric delays are converted to vertical TEC at ionosphere pierce points (IPPs). In the third step, TEC at IPPs is modeled with a spline function to provide the final ionosphere maps. For details on our method, see Krypiak-Gregorczyk et al. (2017a) and Krypiak-Gregorczyk and Wielgosz (2018). Note that we assume the carrier phase bias to be stable in time for a few hours. However, it consists of hardware delays that, according to recent reports, may show some small subdaily variations (Zhang et al. 2017). Nevertheless, our tests demonstrate that the precision of the estimated B_{iGF}^k is better than 1 TECU even under disturbed ionospheric conditions (Krypiak-Gregorczyk and Wielgosz 2018).

The highly accurate and high-resolution model was analyzed for the three tested periods representing the disturbed ionosphere conditions: 1–16 March 2012 (DOYs 61–76), 10–19 March 2013 (DOYs 69–78) and 10–19 March 2015 (DOYs 69–78). For TEC calculation, the data processing from over 200 stations of ground GNSS networks: EUREF Permanent Network (EPN) and European Position Determination System (EUPOS), with 30-s sampling interval and an elevation mask of 30°, was carried out. The mapping of the vertical TEC at the ionospheric pierce point (IPP) locations is based on a single-layer model approach and its associated mapping function (Schaer 1999). Next, a thin-plate splines interpolation is applied for accurate ionospheric TEC modeling and providing the vertical regional TEC maps. These maps are characterized by a 2-min interval and the region limited by -10° and 38° in geographic longitude and 36°

and 64° in geographic latitude, with 0.2° spacing in both directions. The previous results show that the accuracy of these regional TEC maps is better than 1 TEC unit (Krypiak-Gregorczyk et al. 2017b). Note that TEC derived from GNSS data is often denoted as GNSS-TEC. It should be mentioned that since 1 January 2017, we have been providing our results of this European ionosphere model on the Web site http://ginpos.uwm.edu.pl/iono/index_en.php (Krypiak-Gregorczyk et al. 2014).

The quality of the presented highly accurate and high-resolution ionosphere model was tested by a comparison to the broadly used Global Ionosphere Maps (GIMs) provided by the IGS. This commonly available product offers 2.5° by 5.0° spatial resolution and temporal resolution of 2 h. IGS GIMs are developed as an official product of the IGS Ionosphere Working Group by performing a weighted mean of the various Analysis Centers (AC) TEC maps: CODE, ESA, JPL, UPC and NRCAN. According to Hernández-Pajares et al. (2011, 2017), IGS maps are characterized by estimated accuracy ranging from a few TECU to approximately 10 TECU.

Furthermore, an analysis of ionosphere disturbances based on data from the new regional model and IGS reference GIMs was carried out in relation to observations provided from European ionosondes. The behavior of the peak electron density NmF2 during selected periods was analyzed. For this purpose, the critical frequency data (foF2) of the ground-based ionosondes were used to calculate NmF2. It should be noted that foF2 is the most fundamental of all parameters characterizing the state and variations of the ionosphere. These data were provided by the European Digital Upper Atmosphere Server (DIAS). The main goal of the DIAS project is to collect a European digital ionosonde data describing the state of the upper atmosphere, based on real-time information and historical data collections provided by most of the operating ionospheric stations in Europe (Belehaki et al. 2006). The foF2 data is provided with a 15-min time resolution. In the discussed studies, the data from selected two European ionosondes were used due to its availability during the selected disturbed periods. The locations of Juliusruh (54.6°N ; 13.4°E) and Rome (41.8°N ; 12.5°E) ionosondes are presented in Fig. 2.

The GNSS data have been downloaded from the following servers <ftp://cddis.gsfc.nasa.gov/pub/gps/data/daily> and the IGS GIMs from <ftp://cddis.gsfc.nasa.gov/gnss/products/ionex/>. The ionosonde data are available online at <http://dias.space.noa.gr>.

3 Analysis on the ionosphere response to the analyzed storms

The three selected events of the Solar Cycle 24 are characterized by the duration of the shock–sheath–ICME passage

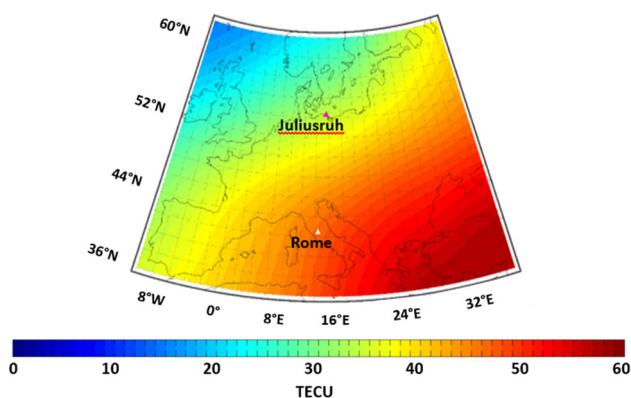


Fig. 2 Example of TEC map derived from UWM model on stormy (DOY 76) day at 9:00 UT, 17 March 2015 and locations of Juliusruh and Rome ionosondes used in the analysis

from ~4 to 9 h. According to Verkhoglyadova et al. (2016), the study of temporal ionosphere responses in global scale needs ionosphere data with temporal resolution of at least 1 h. The study presented in this paper concerns the changes of the ionosphere in a regional scale; hence, an even higher temporal and spatial resolution of the ionosphere maps is necessary. For comparison, the ionospheric TEC variations obtained from well-established IGS GIMs are also presented. For clarity, from this point on, TEC derived from UWM maps is denoted as UWM-TEC, whereas TEC derived from IGS maps is denoted as IGS-TEC.

3.1 Space weather events on March 2012

In order to investigate the ionosphere response to geomagnetic storms in March 2012, the temporal changes of UWM-TEC for the three meridians representing the European region (0°, 12°E and 24°E) were investigated. The meridian 12°E was chosen due to the location of Rome ionosonde whose data were used for this research. Figure 3 presents temporal variations of UWM-TEC for individual 15 grid points of the regional ionosphere maps. Each panel presents UWM-TEC for all analyzed days with respect to average (background) UWM-TEC profiles for quiet days (from 1 to 6 March 2012). The positive phases of the storm (in magenta) and negative ones (in cyan) have been marked in this figure. The largest UWM-TEC was observed at the lowest of the presented latitudes (42°N). According to Tsurutani et al. (2004, 2014) and Mannucci et al. (2005), this effect may indicate the absorption of the electric field contributing to a TEC raise and considerable enhancement at middle latitudes during daytime. In addition, the largest UWM-TEC values have been reached for the longitude 12°E. As it can be seen in all panels, the whole days of 7 and 8 March (DOYs 67, 68) were characterized by positive changes of UWM-TEC.

However, the level of these changes was different depending on the latitude and the UWM-TEC level on the stormy day.

During the disturbed day of 9 March (DOY 69), the highest UWM-TEC was observed at the 42°N latitude. With the increase in the latitude, the UWM-TEC values decreased, reaching the 58°N latitude, a 2.5-fold decrease. In addition, at 50°N latitude, a clear evolution from the negative to the positive phase of the storm is visible. This negative phase of the storm is observed at all analyzed longitudes and latitudes above 50°N. This different nature of the storm on 9 March was associated with an ICME on 7 March that arrived on Earth 2 days later (Belehaki et al. 2017). On the next day, at higher latitudes, the recovery phase followed, and a clear increase in UWM-TEC was visible, while at the lower latitudes, for which the positive phase was observed, UWM-TEC decreases. The reduction of UWM-TEC deepens on 11 March (DOY 71), equating the state of the ionosphere in the quiet period. The event on 12 March (DOY 72) caused a significant 1-day UWM-TEC increase in relation to both the previous day and preceding quiet ionosphere period. The last storm was preceded by increased UWM-TEC, followed by its reduction, bringing the negative phase lasting from sunrise to the afternoon. Then, the positive phase started, which remained until midnight. The next day was characterized by negative changes in the UWM-TEC values, which have reached half of the values of the reference/background period.

The variations of NmF2 observed at the Rome ionosonde from 7 to 16 March 2012 (DOYs 67–76) are presented in Fig. 4. The NmF2 values were recorded every 15 min. The blue line denotes actual NmF2 for all the selected days, and the red line denotes its average value from 1 to 6 March 2012 (quiet background period). The period from 7 to 12 March is characterized by positive disturbances in the NmF2 values in relation to the quiet reference. The NmF2 disturbances turned positive before noon on 7 March (DOY 67), reaching the highest increase in NmF2 at 12:00 UT, amounting to 60% of the quiet-time level. Then, positive changes began to decrease, reaching quiet-time level at about 22:00 UT. However, at this time the NmF2 peaks also occurred at 14:00 and 16:30 UT. Another large increase took place after 6:00 UT. On this day, one can observe two peaks: the first before noon and the second after noon at 14:45 UT. After the second increase in NmF2, there was a reduction in positive changes until 10:15 UT on the next day. Then, the increase in NmF2 took place, reaching the maximum positive change on that day at 13:30 UT. In the following hours, the NmF2 values reached the level of quiet days. On 10 March (DOY 70), positive changes again reached a significant increase at around 11:00 UT. This increase in NmF2 values was close to the level of 7 March. After 16:00 UT, the NmF2 decreased, sometimes presenting the negative phase of the disturbances. On 11 March (DOY 71) from 11:15 UT

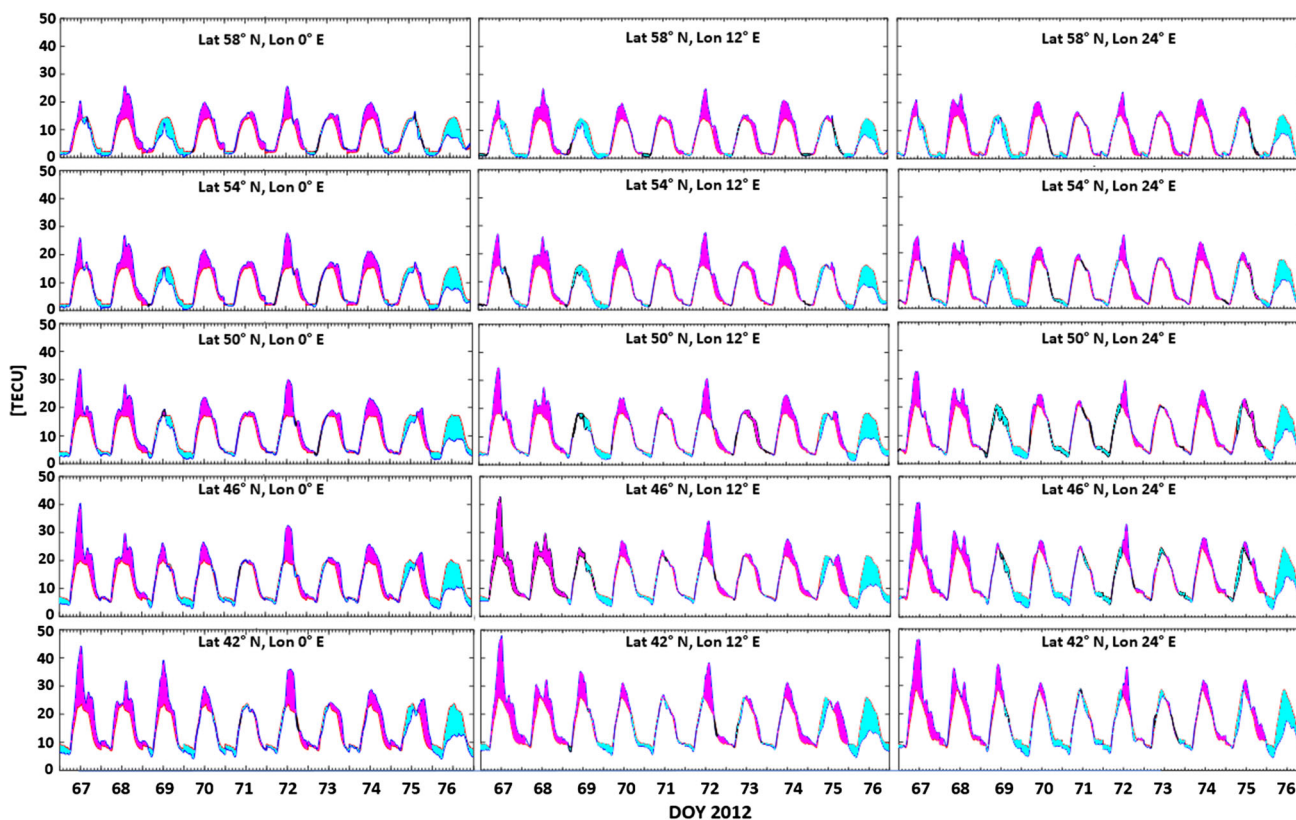
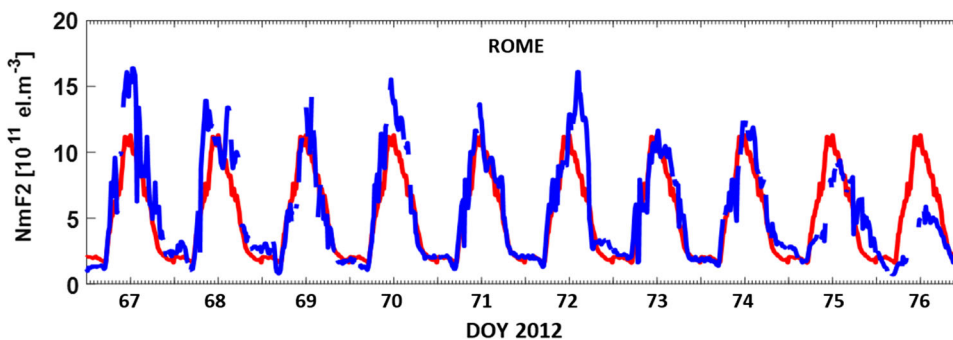


Fig. 3 Variations in the UWM-TEC during the 7–16 March 2012 (DOYs 67–76) with respect to its average for reference quiet days, positive phase of the storm—magenta, negative phase of the storm—cyan

Fig. 4 Variations in NmF2 measured by the Rome ionosonde (the average of NmF2 for quiet days from 1 to 6 March 2012—red line, the NmF2 values for analyzed days—blue line)



to 12:15 UT, an increase in NmF2 was observed in relation to the average of quiet days. In the afternoon only single peaks of positive NmF2 changes were visible. The last large peak of positive changes in the analyzed period was observed on March 12 (DOY 72) at 12:00 UT and remained higher than on quiet days until 17:15 UT. Then NmF2 decreased to the quiet period level. The storm, which took place on March 15 (DOY 75), was characterized by a clear decrease in NmF2 starting from 5:45 UT. These negative disturbances lasted until 16:45 UT. Next, the NmF2 disturbances turned positive and persisted until midnight, but the whole day after the storm was characterized by negative changes in NmF2.

Figure 5 presents a comparison of the differential TEC derived from new regional UWM maps and IGS GIMs during the analyzed period (7–16 March 2012). The top panel shows the differential map providing the information about the difference of UWM-TEC during the stormy period in relation to the background quiet days (1–6 March 2012), calculated as $\Delta\text{TEC} = \text{TEC}_{\text{storm}} - \text{TEC}_{\text{quiet}}$. These maps are derived for 13°E longitude, as this is an average for both ionosondes. The maps show clear TEC increase during disturbances on 7, 9, 12 and 15 March 2012 (DOYs 67, 69, 72, 75). Each of these events is characterized by a positive phase of the storm at about the same time at all latitudes. The largest positive effect of the analyzed storms can be observed on 9

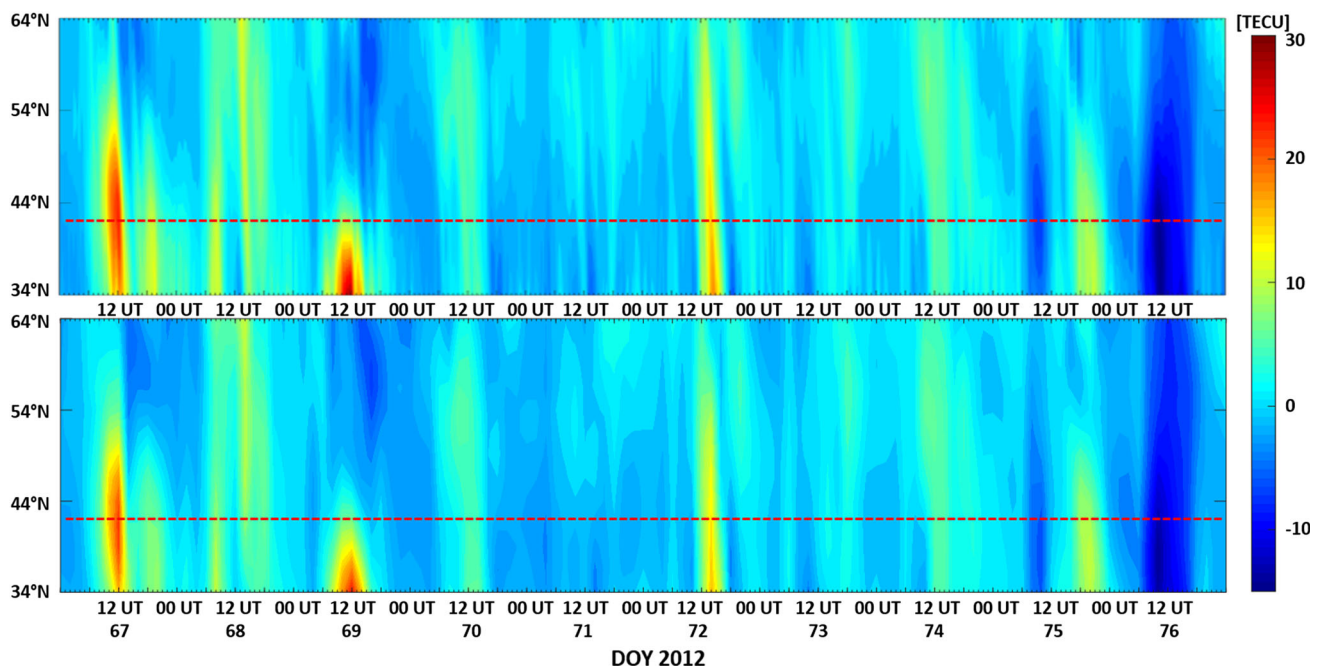


Fig. 5 Differential UWM-TEC (top panel) and IGS-TEC (bottom panel) maps for 13°E longitude during the stormy period (7–16 March 2012/DOYs 67–76) in relation to the background quiet days (the red dotted line reflects the location of the Rome ionosonde)

March 2012 (DOY 69). There was a significant increase in the UWM-TEC; however, larger positive disturbances occurred at lower latitudes. The other stormy events were characterized by moderate positive disturbances. In addition, this map shows that the positive phase of the storm on 15 March (DOY 75) was preceded by a decrease in the UWM-TEC values from about 11:00 UT at all latitudes. This positive phase began at around 18:00 UT and lasted until 22:00 UT. The UWM-TEC increase was observed only up to 57°N latitude. On the next day, at about 8:00 UT one can observe a decrease in UWM-TEC lasting until 18:00 UT. This was the largest decrease in the UWM-TEC in the analyzed period.

The bottom panel presents the differential map providing the information about the IGS-TEC. The general nature of the observed changes during the analyzed period shows compatibility with UWM-TEC. However, the level of IGS-TEC variations during these storms is clearly lower, and its maximum differences occur at lower latitudes than in the case of the new model.

As it is well known, GNSS-TEC is the integrated number of electrons along the radio wave propagation path from the GNSS satellites to the receiver. Hence, it is clear that this parameter depends to a large extent on the peak electron density in F layer (NmF2). Therefore, the response of the ionosphere to the disturbances perceived in terms of the NmF2 and GNSS-TEC should be to some extent similar. It is a commonly accepted assumption that TEC and NmF2 are highly correlated, and thus, TEC can be used for studies of F2 layer dynamics (Mendillo 2006; Prolss 2006; Zolotukhina et al.

2017). However, it should be emphasized that approximately two-third of TEC comes from the topside ionosphere. This is a region above the ionization maximum (Mendillo 2006; Liu et al. 2016). According to Yizengaw et al. (2006) and Astafyeva et al. (2015), the F layer and the topside ionosphere do not always react in the same manner during geomagnetic storms. Many authors have proven that the TEC variation depends on ionospheric peak density variability, topside electron density and temperature fluctuations, and changes in the plasmasphere (Klimenko et al. 2015; Liu et al. 2016).

For clarity, red dotted line at 42°N latitude was plotted in the differential maps. This line reflects the location of the ROME ionosonde. In the next step, profiles of differential UWM-TEC and IGS-TEC for this latitude were subjected to temporal analyses. Due to 15-min time resolution of the foF2 data, the temporal profiles from UWM and IGS maps were also created with a 15-min interval. Figure 6 presents the differential UWM-TEC profiles (top panel) and IGS-TEC profiles (middle panel) during the stormy period (7–16 March 2012/DOYs 67–76) in relation to the background quiet days. The bottom panel presents the differences of F-layer maximum electron density measured by the ionosonde in Rome. The nature of NmF2 changes during the storm corresponds to both UWM-TEC and IGS-TEC changes for latitude of 42°N. During the analyzed period, both positive and negative disturbances observed by UWM map and IGS GIMs have a very high compatibility with the differences of NmF2. Despite the general compatibility of the presented profiles from UWM and IGS maps, the former one presents a higher

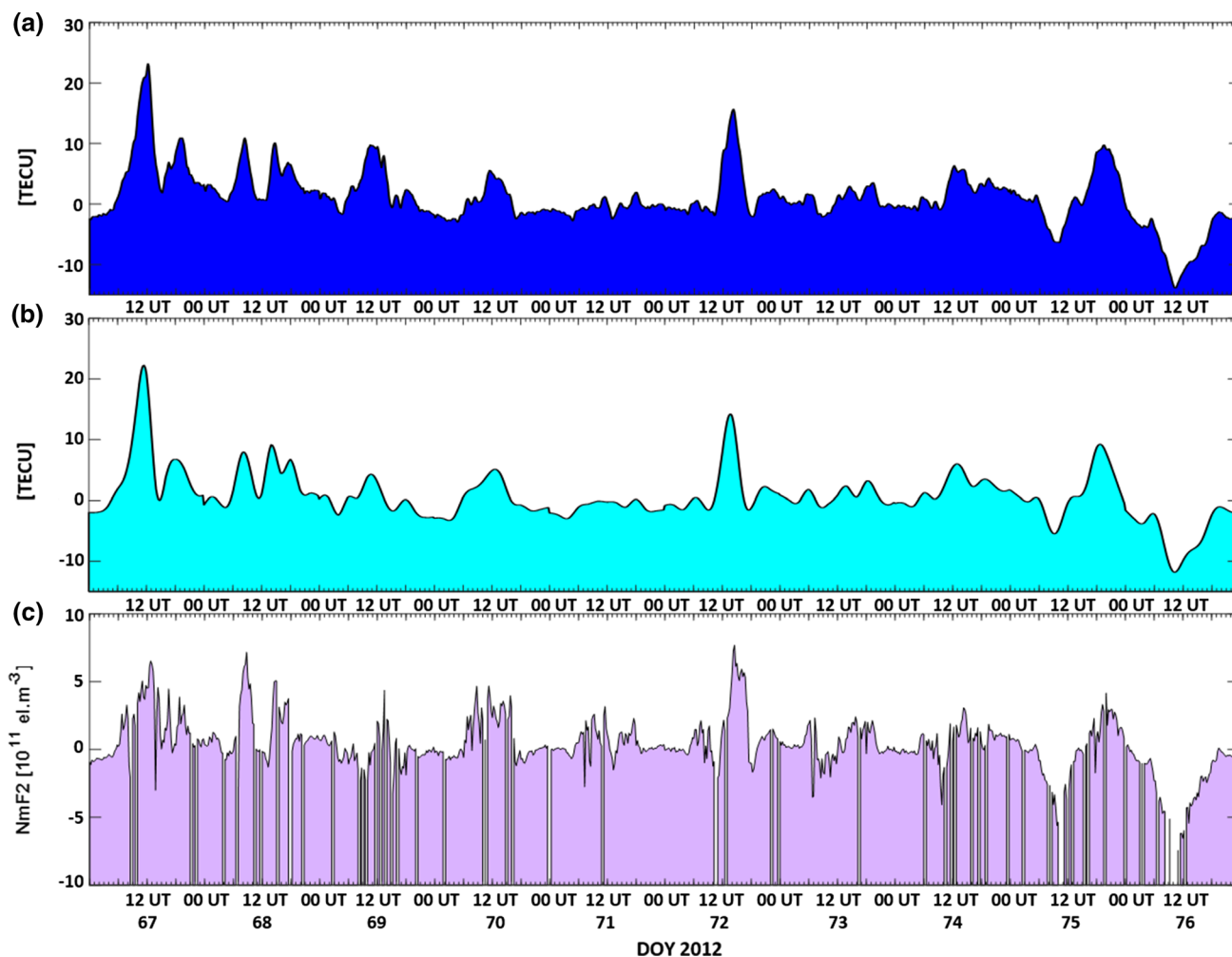


Fig. 6 Profiles of differential UWM-TEC (a), IGS-TEC (b) and NmF2 (c) for the location of the Rome ionosonde during the stormy period (7–16 March 2012/DOYs 67–76) in relation to the background quiet days

level of detail similarly to the ionosonde data. The IGS-TEC reflects only the general nature of changes, while the high-resolution model is characterized by a better representation of the dynamics of changes in the ionosphere.

3.2 Space weather event on March 2013

The general behavior of UWM-TEC at different latitudes for 17–19 March 2013 (DOYs 76–78) covering the geomagnetic storm (17 March, DOY 76) and 2 days after this event is shown in Fig. 7. As a reference to the analysis, a quiet ionosphere background period from 10 to 16 March 2013 was selected, and the average UWM-TEC of these quiet days was calculated. On the stormy day, the increase in UWM-TEC can be observed in all cases. The highest level of UWM-TEC was observed at the lowest latitude of 42°N in all three analyzed longitude sectors. On the dayside, positive UWM-TEC deviations reaching 55 TECU with a double peak structure are observed. This second peak occurred during

the MC passage (Verkhoglyadova et al. 2016). This behavior of the ionosphere is observed up to 50°N latitude. The decrease in UWM-TEC with respect to the average of quiet days started at midnight on 18 March (DOY 77) and lasted for two consecutive days. Above 50°N latitude, the positive effect is visible from 8:00 UT and lasts until 16:00 UT. Then, with the decrease in UWM-TEC, the negative phase of the storm begins. A slight increase in UWM-TEC in relation to the reference values is observed only from 16:00 UT to 20:00 UT on 18 March. On the higher latitudes, the positive effect is also observed from 20:00 UT on 17 March (DOY 76) to the sunrise on 18 March (DOY 77).

The response of the ionosphere to this event at the latitudes of 42°N and 54°N was analyzed based on the variations in the F-layer maximum electron density measured by the ionosondes in Rome and Juliusruh. These changes are presented in Fig. 8, where the blue line corresponds to the changes in the disturbed period, and the red line is the average of the quiet days. The bottom panel shows changes in the NmF2

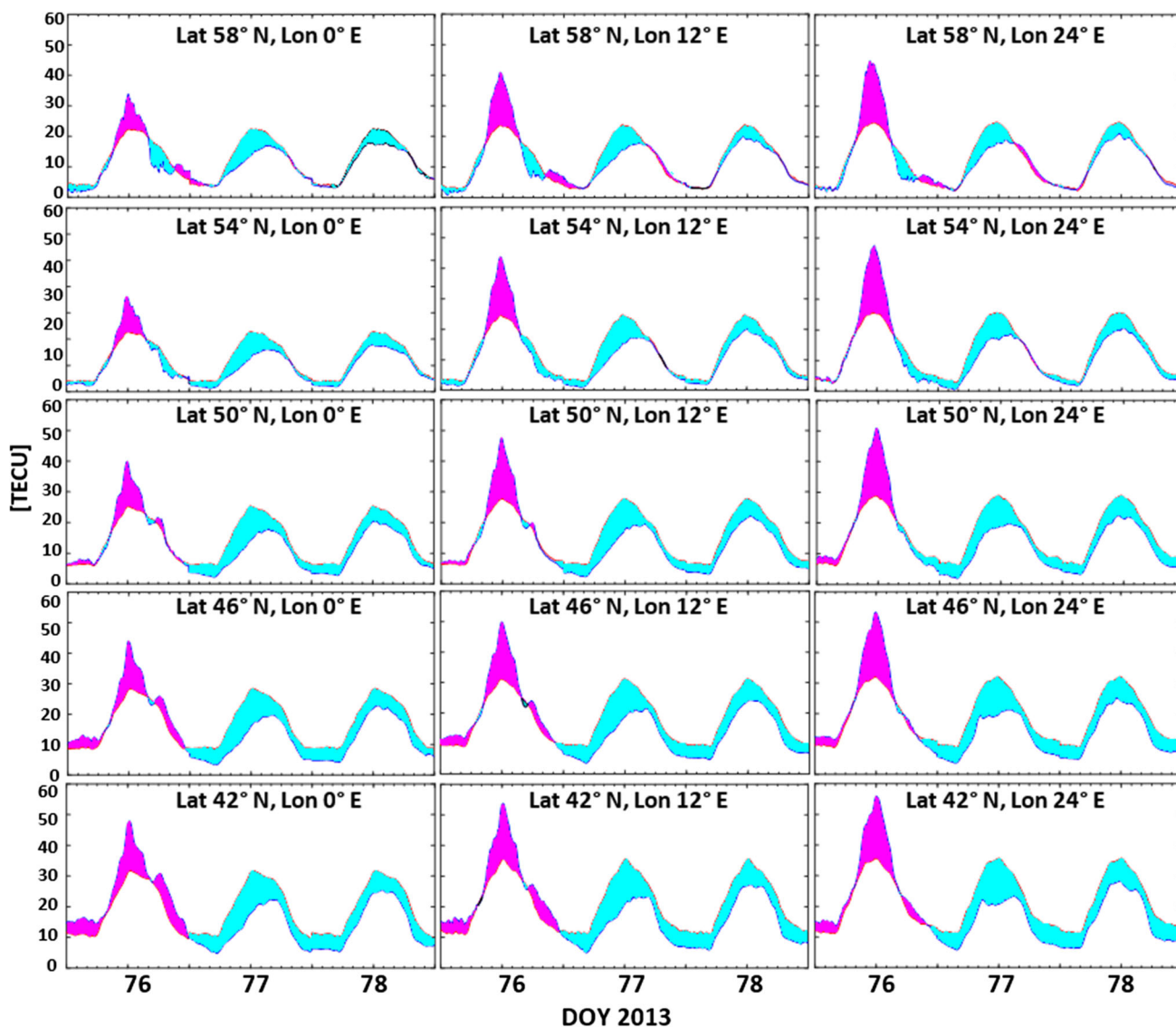


Fig. 7 Variations in UWM-TEC during 17–19 March 2013 (DOYs 76–78) with respect to its average reference quiet days, positive phase of the storm—magenta, negative phase of the storm—cyan

measured by the Rome ionosonde. These values began to increase in relation to the respective reference values on 17 March at sunrise. This condition lasted until the end of the day. The maximum NmF2 was reached at 12:00 UT, then started to decrease, and another increase occurred at about 18:00 UT. The positive phase lasted until midnight; then, NmF2 started to decrease in relation to the reference values, and the negative phase was continued for the next 2 days. These observations correspond well with the UWM-TEC changes obtained from the new regional ionosphere maps.

The top panel in Fig. 8 shows the variations in the F-layer maximum electron density measured by Juliusruh ionosonde. The positive phase of the storm started at 8:00 UT and lasted until 16:00 UT. Then, the UWM-TEC values fell below the

reference level and the negative phase lasted for the next 2 days. The observed disturbances correspond to the changes of UWM-TEC presented in Fig. 7, in the panel describing the disturbances at 54°N latitude and the 12°E longitude.

In the next step, the differential UWM-TEC and IGS-TEC were compared. Top panel in Fig. 9 shows the differential UWM-TEC map, while the differential IGS-TEC map is presented in the bottom panel. These maps provide information about TEC variations during the stormy day and two subsequent days in relation to the background ionosphere (10–16 March 2013). Both models present an evident TEC increase on the stormy day at all latitudes. The increase began at 8:00 UT, and the positive phase of the storm reached its peak at 12:00 UT. However, the highest positive effect was observed at latitudes below 54°N for IGS-TEC, while

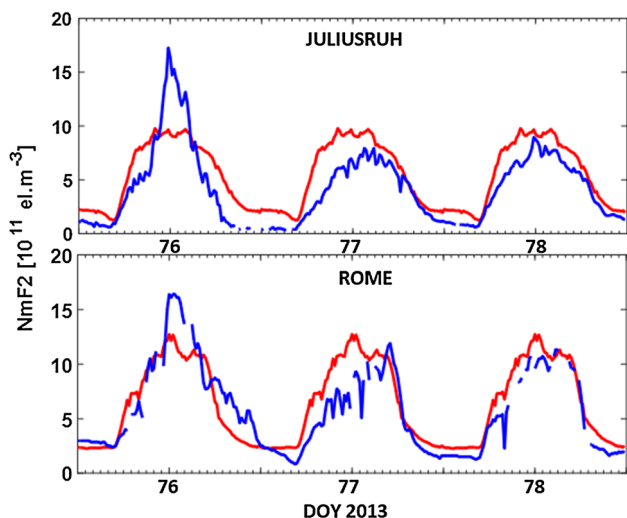


Fig. 8 Variations in NmF2 measured by the ionosondes in Rome and Juliusruh (average of NmF2 for quiet days from 10 to 16 March 2013 (DOYs 76–78)—red line, NmF2 values for analyzed days—blue line)

the differential UWM-TEC data reached the highest values at about 54°N. In the afternoon, these changes were getting close to zero at 15:00 UT.

Then, in the case of IGS map, TEC had been increasing from 16:00 UT, reaching the second peak around 19:00 UT. The UWM map observed this increase a little later. However, this second peak also occurred at around 19:00 UT. For both models, this peak was characteristic only at latitudes below 44°N, and its maximum value occurred at latitudes below 36°N. In addition, the second peak in TEC amounted to 50% of its level observed during the first peak. Despite the overall compatibility of the changes in the ionosphere observed by

both TEC maps, there is a clear difference in the character of the second peak, with TEC fluctuations seen in UWM-TEC.

The next day was characterized by the negative phase at all latitudes, and the largest negative changes were observed at 12:00 UT, for both models. On this day, there are significant differences in TEC variations presented by both models. These negative changes also continued on the following day, but the level of TEC changes was much lower. In the case of UWM-TEC, the storm recovery phase is clearly visible, while IGS-TEC almost does not reflect this phase of the storm. Figure 9 shows the clear differences in the ionosphere response to the analyzed geomagnetic storm.

In addition, the ionospheric TEC behavior was also evaluated against variations of NmF2 measured by ground ionosondes in Rome and Juliusruh. The red dotted line reflects the location of the Rome ionosonde, and the blue dotted line reflects the location of the Juliusruh one. The top and middle panels in Fig. 10 present the UWM-TEC and IGS-TEC profiles for the location of Juliusruh, while the bottom panel shows the differences of NmF2 measured by the ionosonde in Juliusruh. As is evident, UWM-TEC profiles better follow NmF2 variations, as compared to IGS-TEC. In all of the analyzed profiles, the positive storm phase is clearly visible and reached a peak at 12:00 UT on the first stormy day. On the next day, there is a sharp drop in TEC values starting around 6:00 UT. This drop in the case of IGS-TEC is rather gentle, while UWM-TEC presents more rapid decrease, which reflects the effect visible in the ionosonde profile. Furthermore, on the third day at 6:00UT, both UWM and ionosonde profile present a sharp gradient in the ionosphere, while again in the case of IGS-TEC this gra-

Fig. 9 Differential UWM-TEC (top panel) and IGS-TEC (bottom panel) maps for 13°E longitude during the stormy period (17–19 March 2013/DOYs 76–78) in relation to the background quiet days (the red dotted line reflects the location of the Rome ionosonde, and the blue dotted line reflects the location of the Juliusruh ionosonde)

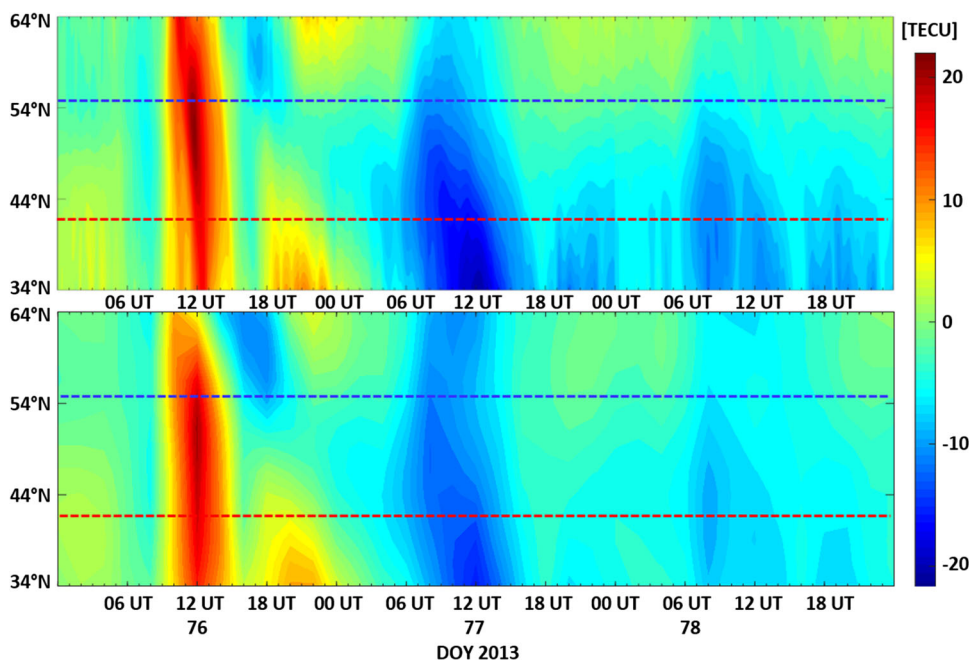


Fig. 10 Profiles of differential UWM-TEC (a), IGS-TEC (b) and NmF2 (c) for the location of the Juliusruh ionosonde during the stormy period (17–19 March 2013/DOYs 76–78) in relation to the background quiet days

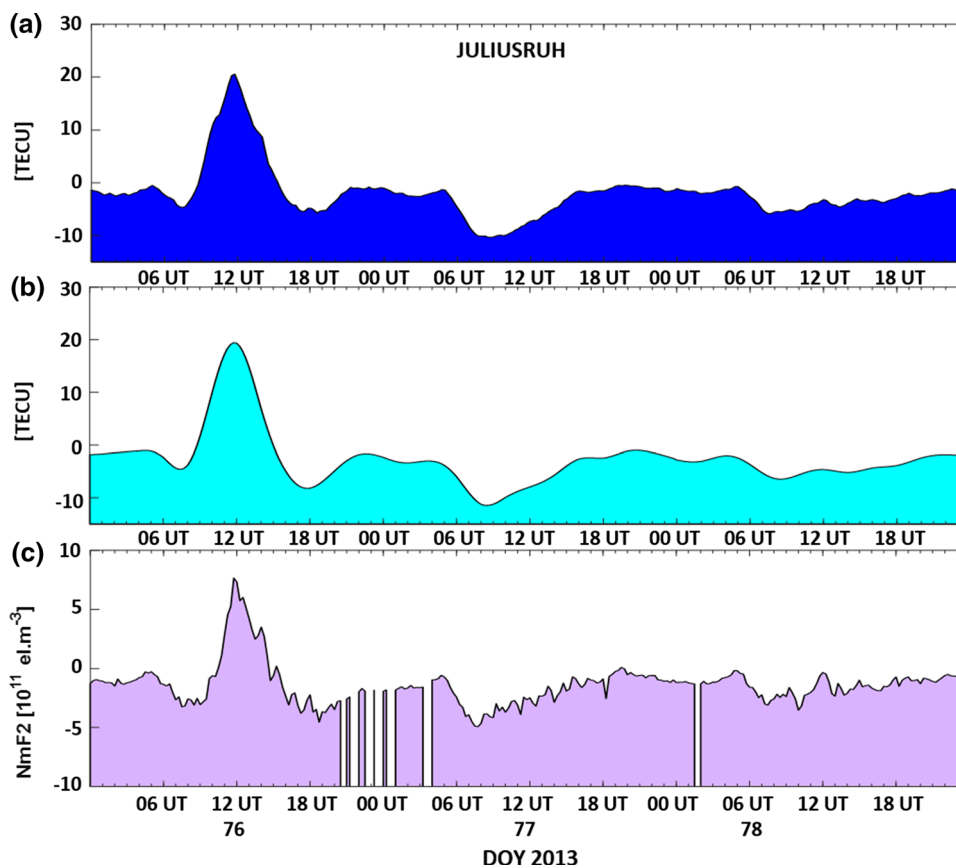
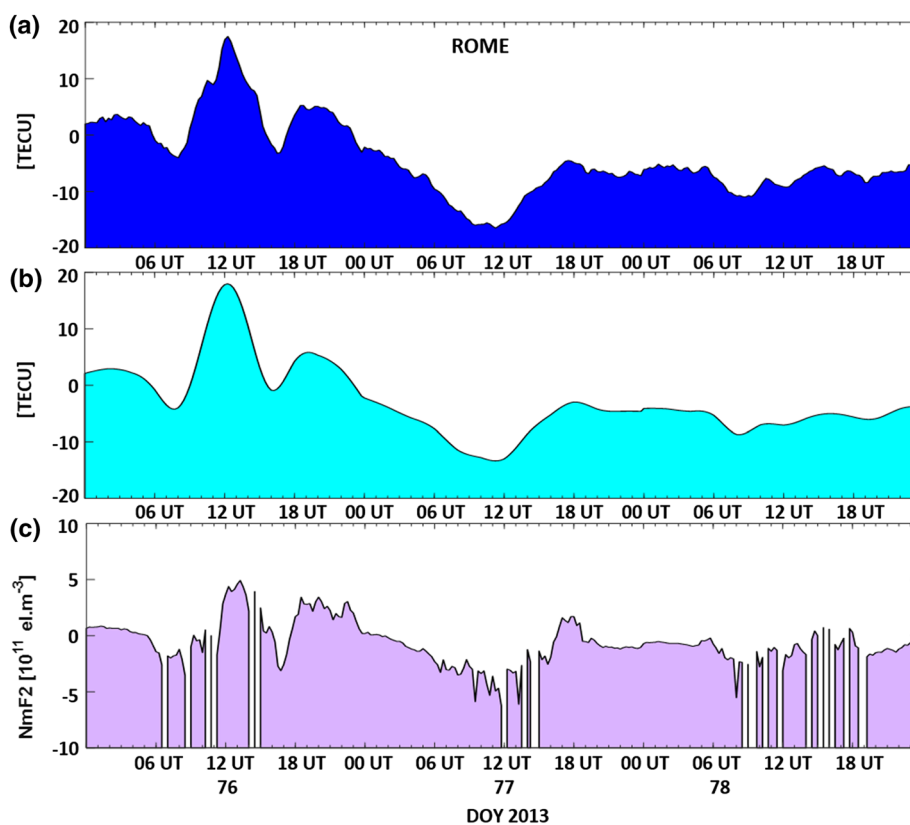


Fig. 11 Profiles of differential UWM-TEC (a), IGS-TEC (b) and NmF2 (c) for the location of the Rome ionosonde during the stormy period (17–19 March 2013/DOYs 76–78) in relation to the background quiet days



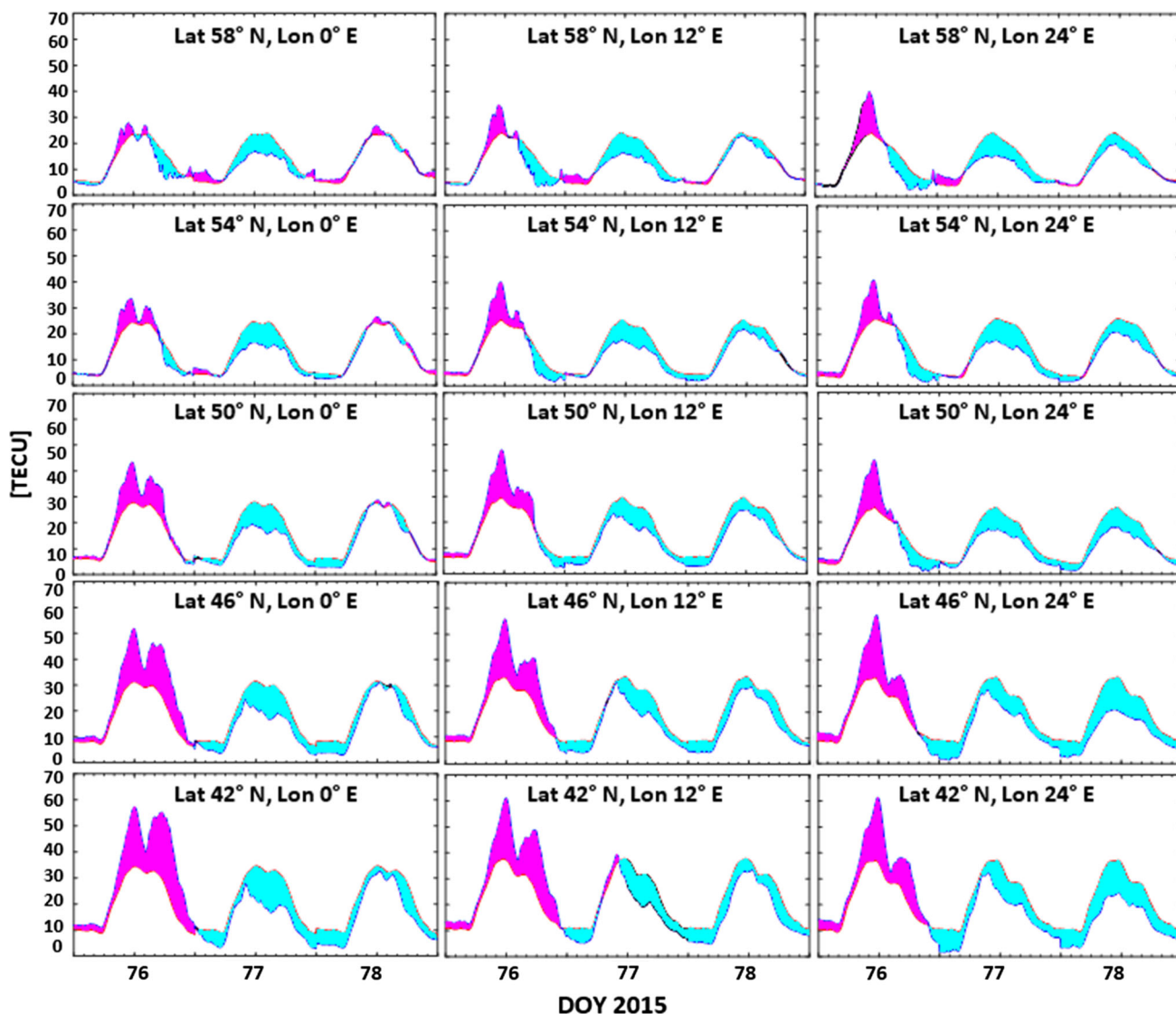


Fig. 12 Variations in UWM-TEC during the 17–19 March 2015 (DOYs 76–78) with respect to its average for the reference quiet days, positive phase of the storm—magenta, negative phase of the storm—cyan

dient is less pronounced. Also, on 19 March, both TEC and NmF2 relative values approached zero, reflecting the recovery phase. Moreover, despite the general compatibility of the profiles, it can be stated that the UWM-TEC profile better describes the ionosphere response to the storm, as compared to the ionosonde data.

Figure 11 shows the profiles of differential TEC from UWM map (top), IGS map (middle) and NmF2 (bottom) for the location of the Rome ionosonde. As one can see, ionosphere variations have a different character than those observed for the Juliusruh ionosonde. The nature of the TEC changes observed during the three analyzed days corresponds to the NmF2 variations over Rome. The positive as well as negative phases of the storm show great compatibility. During the storm, the TEC profiles present two peaks: the first

one after 12:00 UT and the second one after 18:00 UT. The next day was characterized by the negative phase observed by both models and the ionosonde, and the largest negative changes were observed at 9:00 UT. On the following day, the storm recovery phase is clearly visible in all profiles. Nevertheless, the profiles created from the UWM maps for the Juliusruh and Rome ionosondes show clearly more details, thus closer reflecting the response of the ionosphere to the disturbances.

3.3 Space weather event on March 2015

The general dynamics of ionospheric disturbances over Europe during the Saint Patrick storm (2015) is shown in Fig. 12. The reference quiet ionosphere was obtained as

UWM-TEC average from 10 to 16 March 2015. After the commencement of the main phase of the storm ($\sim 7:30$ UT), the first UWM-TEC enhancement is visible on all analyzed grid points. During the next 4 h, UWM-TEC at 42°N latitude increased twice, reaching a peak at around 12:00 UT. As the latitudes increases, the UWM-TEC level decreases. However, for all peak points, UWM-TEC is twice as large as at the start of the main storm phase. At the latitudes above 54°N , the peak values were reached at around 11:00 UT. In all the analyzed cases, this positive storm phase is very clearly visible. The observed UWM-TEC variations correspond to the coronal loop passage, and the increase in the electron content corresponds to the sheath passage (Verkhoglyadova et al. 2016). After reaching its peaks, UWM-TEC decreased, approaching the background values, and at the 58°N latitude reached values below this level. Then, there was a pronounced increase in UWM-TEC, leading to the second peak of this day. At the latitudes of 42°N and 46°N , the peak values were reached at around 18:00 UT. Then, there was a decrease in UWM-TEC visible during a MC passage. At these latitudes, the positive phase turned into the negative phase at around 22:00 UT and remained so for the next 2 days. However at 12°E , a positive storm phase appeared again at about 5:00 UT; however, it was a minor one. Next, at about 11:00 UT, UWM-TEC started to drop again and the negative storm phase lasted until the end of the analyzed period. At 50°N latitude and above, the second peak of UWM-TEC was reached after 14:00 UT. At latitude 54°N and at 58°N , the peak slightly exceeded the average quiet-time level. Moreover, at higher latitudes there is no positive phase of the storm before noon on 18 March (DOY 77), but only a small, several-hour increase in UWM-TEC above the background level after midnight, on 17/18 March (DOY 76/77) and 18/19 March (DOY 77/78).

In the case of this event, as during the storm of 2013, the variations in the F2 layer maximum electron density observed by Juliusruh and Rome ionosonde were analyzed. The changes in the NmF2 values derived from the Rome ionosonde are presented in the bottom panel in Fig. 13. The positive phase of the storm is clearly visible with two peaks on the disturbed day at 12:00 UT and 18:00 UT on 17 March 2015 (DOY 76), which perfectly correspond to the UWM-TEC peaks. In the case of ionosondes data, one more peak at around 22:00 UT is clearly visible, which was not observed in the TEC maps. In addition, on 18 March (DOY 77) at sunrise, an increase in the NmF2 values is observed, lasting until around 10:00 UT. Then, the peak was reached, followed by a NmF2 sudden decline and the negative phase of the storm began, lasting until the end of the analyzed period.

With regard to the changes in NmF2 measured by the Juliusruh ionosonde, a significant increase is visible after 10:00 UT on the disturbed day, reaching its peak before noon. Then, the NmF2 values decrease and the negative phase of the

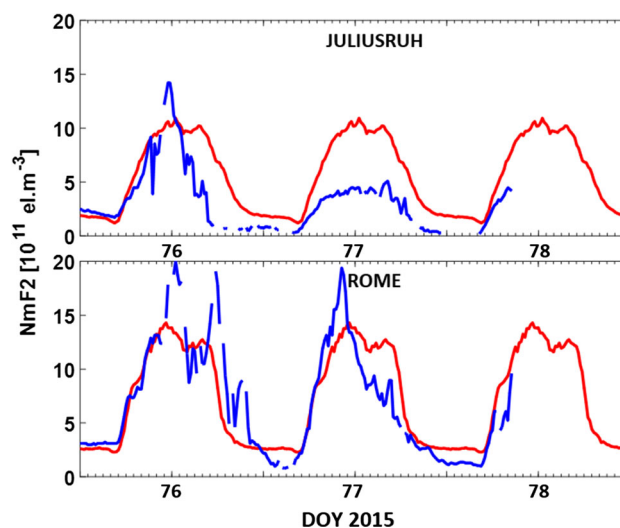
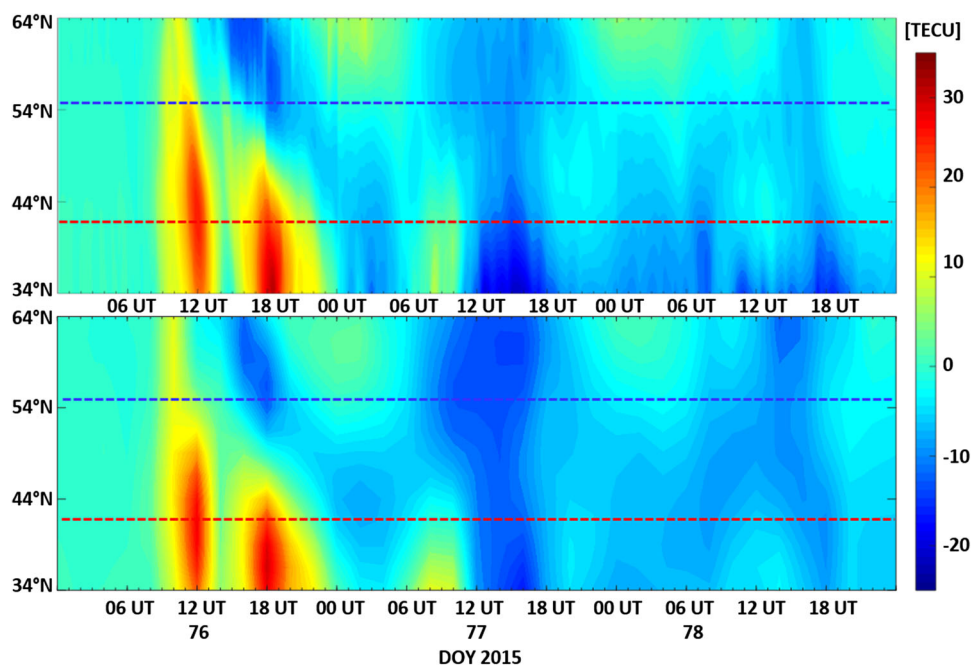


Fig. 13 Variations in NmF2 measured by ionosondes in Rome and Juliusruh (the average of NmF2 for quiet days from 10 to 16 March 2015 (DOYs 76–78)—red line, the NmF2 values for analyzed days—blue line)

storm began, which lasted for the next 2 days. A significant 50% decrease in NmF2 was observed. Only at sunrise on 18 and 19 March, there was a short-lived increase in the analyzed NmF2, approaching the level from the quiet period. The discussed variations of the electron density observed by the Juliusruh ionosonde correspond with the changes of UWM-TEC for the location of this ionosonde.

As in the case of earlier storms, the differences in UWM-TEC and IGS-TEC have been analyzed. TEC variations on 17 March 2015 (DOY 76) and two subsequent days are presented in Fig. 14 in relation to the average/background quiet days (10–16 March 2015). The first increase in UWM-TEC is visible at about 09:00 UT at all latitudes. This event was observed until 13:00 UT for both models. However, the peak in UWM-TEC is visible at latitudes below 56°N , while the corresponding peak in IGS-TEC occurs below 50°N only. Then at around 14:00 UT, a short-term UWM-TEC decrease was observed. From about 16:00 UT, a positive UWM-TEC deviation was observed at latitudes below 54°N and below 46°N for IGS-TEC, reaching in both cases the highest values at 18:00 UT. From 20:00 UT, the disappearance of the positive phase is noticeable. Starting from 01:00 UT on March 18 (DOY 77), the negative phase of the storm began to appear at lower latitudes. Between 01:00 UT and 07:00 UT, the deviations of UWM-TEC with respect to the background period had vanished. Next, both models observed an increase in differential TEC values. Then from 11:00 UT on, a strong negative storm started to dominate at the most latitudes in the IGS map, whereas for UWM-TEC, the negative storm phase was clearly visible at the latitudes below 44°N only. At the end of the day, the negative changes started

Fig. 14 Differential UWM-TEC (top panel) and IGS-TEC (bottom panel) maps for 13°E longitude during the stormy period (17–19 March 2015/DOYs 76–78) in relation to the background quiet days (the red dotted line reflects the location of the Rome ionosonde and the blue dotted line reflects the location of the Juliusruh ionosonde)



to be less visible for both models. This condition persisted for the greater part of the next day. In addition, at about 18:00 UT at latitudes below 44°N, in the case of UWM-TEC, there was a sudden short-lived increase in the negative effects.

As in the case of the storm of 2013, the profiles of differential TEC for location of the Juliusruh ionosonde show a slightly different nature of the storm as observed by two independent models (Fig. 15). It should be noted that the deviations of NmF2 observed by the Juliusruh ionosonde largely reflect the same nature of ionosphere variations that can be observed from UWM-TEC. At about 10:00 UT, a temporary drop in the electron content followed by a second peak 2 h later is observed only in the case of UWM-TEC and ionosonde profiles. While the positive storm phase is observed in all profiles, UWM-TEC and ionosonde data show its peak at about 11:00 UT. And this peak is visible one hour earlier in the IGS-TEC profile. Moreover, the IGS-TEC profile shows a smooth decrease in the TEC values, which does not reflect the dynamic nature of changes in the ionosphere presented in other profiles. For instance, a small peak at 6:00 UT on the second day is completely missing in the IGS data. On that day, from about 8:00 UT to 15:00 UT, the negative phase of the storm is clearly visible in all profiles. However, UWM and Juliusruh ionosonde profiles detect small changes in the slope that are not present in IGS-TEC. Nevertheless, all profiles present the similar ionosphere response after 15:00 UT.

In the case of the Rome ionosonde data, the analyses are more difficult due to frequent gaps in NmF2 data during

the two main peaks in the electron density (Fig. 16). The presented differences reflect the positive phase of the storm in all profiles. The first peak is observed at 12:00 UT and the second at 8:00 UT on the second day. In addition, a sudden appearance of the negative phase of the storm on 18 March is well marked in all profiles. However, the IGS-TEC profile shows rather smooth changes taking place in the ionosphere, while UWM-TEC presents some finer structures, similar to the ionosonde data.

In addition, the correlation coefficients between variations of NmF2 and TEC derived from UWM and IGS maps were calculated. Table 1 shows that the correlations between variations of NmF2 and UWM-TEC during all analyzed periods are higher than between NmF2 and IGS-TEC. The advantage of UWM-TEC is more pronounced in case of mid-latitude ROME ionosonde, though the correlation never exceeds 82%. However, according to Liu et al. (2016), in fact TEC variations do not always correlate well with NmF2 variations during geomagnetic storms, due to the TEC variability dependent on the lower and topside ionosphere as well as the plasmasphere.

4 Discussion and summary

The three discussed geomagnetically active periods occurred during the same solar illumination conditions. All of them took place near the spring equinox, and moreover, the events in 2013 and 2015 occurred on the same day of the year. This leads to similar ionospheric conductivity profiles; however,

Fig. 15 Profiles of differential UWM-TEC (a), IGS-TEC (b) and NmF2 (c) for the location of the Juliusruh ionosonde during the stormy period (17–19 March 2015/DOYs 76–78) in relation to the background quiet days

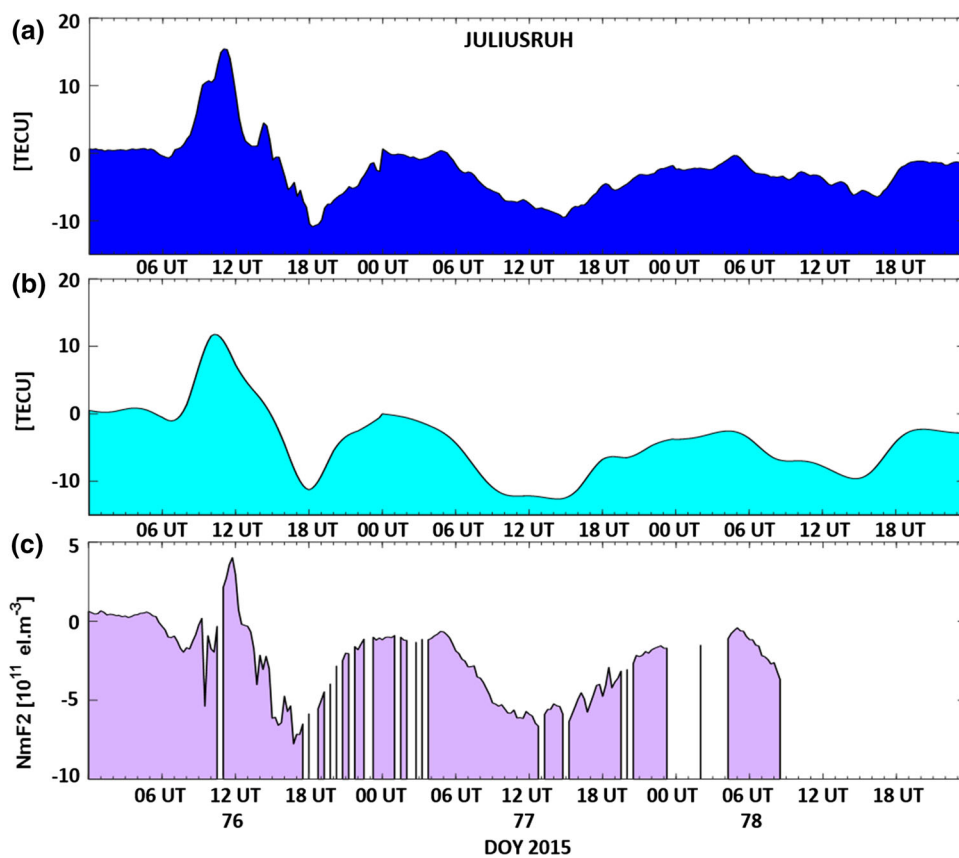


Fig. 16 Profiles of differential UWM-TEC (a), IGS-TEC (b) and NmF2 (c) for the location of the Rome ionosonde during the stormy period (17–19 March 2015/DOYs 76–78) in relation to the background quiet days

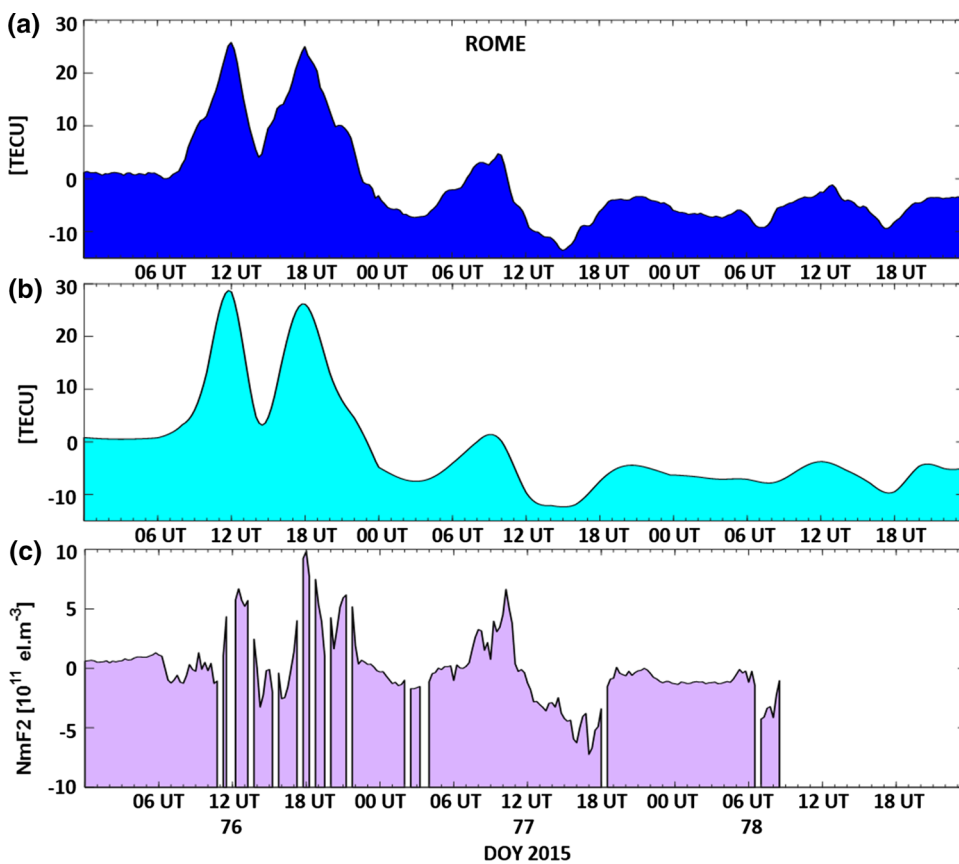


Table 1 Correlations between NmF2 variations and both UWM-TEC and IGS-TEC during all analyzed periods

Model	Storms					
	7–16 March 2012		17–19 March 2013		17–19 March 2015	
	Juliusruh	Rome (%)	Juliusruh (%)	Rome (%)	Juliusruh (%)	Rome (%)
UWM	–	77	81	82	82	80
IONEX	–	70	78	69	81	74

these storms are associated with very different IMF conditions.

The presented storms have been analyzed to assess the capability of the new regional ionospheric model to reproduce complex behavior of the ionosphere. The general impact of space weather events on the total electron content over Europe is presented in Sect. 3. The analysis of the temporal changes taking place in the ionosphere showed a very good agreement between the results provided by our regional ionosphere model and those derived from the ionosondes. In general, the nature of the temporal ionosphere changes observed with the use of two independent sources was very similar. To further investigate the ionospheric disturbances during the selected storm event, the detailed variations of the UWM-TEC values on stormy days are presented in Figs. 17 and 18. These maps showing the storm-time response of the ionosphere over Europe were derived as an average over European sector (from 10°W to 35°E).

Figure 17 shows maps of local time–latitude UWM-TEC distributions for four events on 7, 9, 12 and 15 March 2012. Figure 17a presents a typical behavior of the ionosphere during stormy days. Again, as a reference, a quiet period of the ionosphere from 1 to 6 March 2012 was selected. The middle panel (b) presents the UWM-TEC distribution during stormy days on March 2012. Note that the maps showing the quiet and disturbed ionosphere are presented in the same scale. The maps of differences between an active and quiet ionosphere are presented in the bottom panel, and a different scale is used.

It should be emphasized that at 4:30 UT on 7 March there was an increase in auroral activity, and according to Pross (1995) this should have immediately triggered a negative storm phase. However, in this case it did not happen. The rising TEC reached its peak at about 11:00 LT at latitudes above 40°N, and then, the highest values in daytime were achieved at noon at latitudes lower than 40°N. This effect may indicate the dayside super-fountain effect. According to Tsurutani et al. (2014), the absorption of the electric field contributes to TEC decrease at the magnetic equator during dusk local times, and to its rise and considerable enhancement at middle latitudes during daytime (Tsurutani et al. 2004; Mannucci et al. 2005; Tsurutani et al. 2014). After 14:00 LT, as in Belehaki et al. (2017), the bulge of the composition is visible, starting in the auroral zone. It can be presumed that this is

the effect of substorm intensification. On this day, there was the second peak of TEC level at around 18:00 LT.

The differential UWM-TEC map provides more information about the occurred disturbances, clearly showing the above-mentioned TEC peaks. As presented in Fig. 17, the storm on 9 March had a completely different nature than on 7 March. A clear TEC increase is observed during daytime, the largest one in this period. The TEC values began to grow at sunrise, reaching the highest level at around 11:30 LT at latitudes below 40°N. The differential map confirmed a significant increase in UWM-TEC on this day, emphasizing more than a two-time increase in TEC at low latitudes (below 36°N).

The next disturbed day (12 March) was characterized by a sudden increase in TEC at about 10:30 LT, reaching peak values at about 11:00 LT. A rapid decrease in TEC was observed from 15:00 LT. This phenomenon is perfectly reflected by the differential map. The last disturbance, characterized by the smallest TEC changes, presents a completely different response of the ionosphere. The map showing this disturbed day clearly indicates two TEC peaks: the first peak occurred after 12:00 LT and the second one at around 18:00 LT. The analysis of the differential map confirms the occurrence of these anomalies. In addition, Fig. 17 reveals that the increase in the TEC value was preceded by a reduction of TEC after 6:30 LT at all observed latitudes. At around 13:00 LT, at latitudes below 42°N, there was a slight increase in TEC values in relation to its average for quiet days. While the second peak at around 18:30 LT is clearly visible, the increased TEC lasted until the end of the day.

UWM-TEC disturbance dependency on time and latitude for two St. Patrick storms in 2013 and 2015 is presented in Fig. 18. The top panel shows the typical behavior on quiet days as reference for March 2013 and 2015. This reference is derived from average ionosphere for quiet days from 10 to 16 March for each year. At latitudes lower than 40°N, the second TEC peak appeared at around 16:00 LT. In order to study the storm-time response of the ionosphere, the TEC variations during the magnetic storm on 17 March 2013 are presented in the middle panel. Morning TEC did not show any pronounced storm-driven effects. During a sheath passage, there is an increase in TEC at midlatitudes. Its maximum was achieved at 11:00 LT in the north (60°N), and just before noon in the south (34°N). As presented in Verkhoglyadova et al.

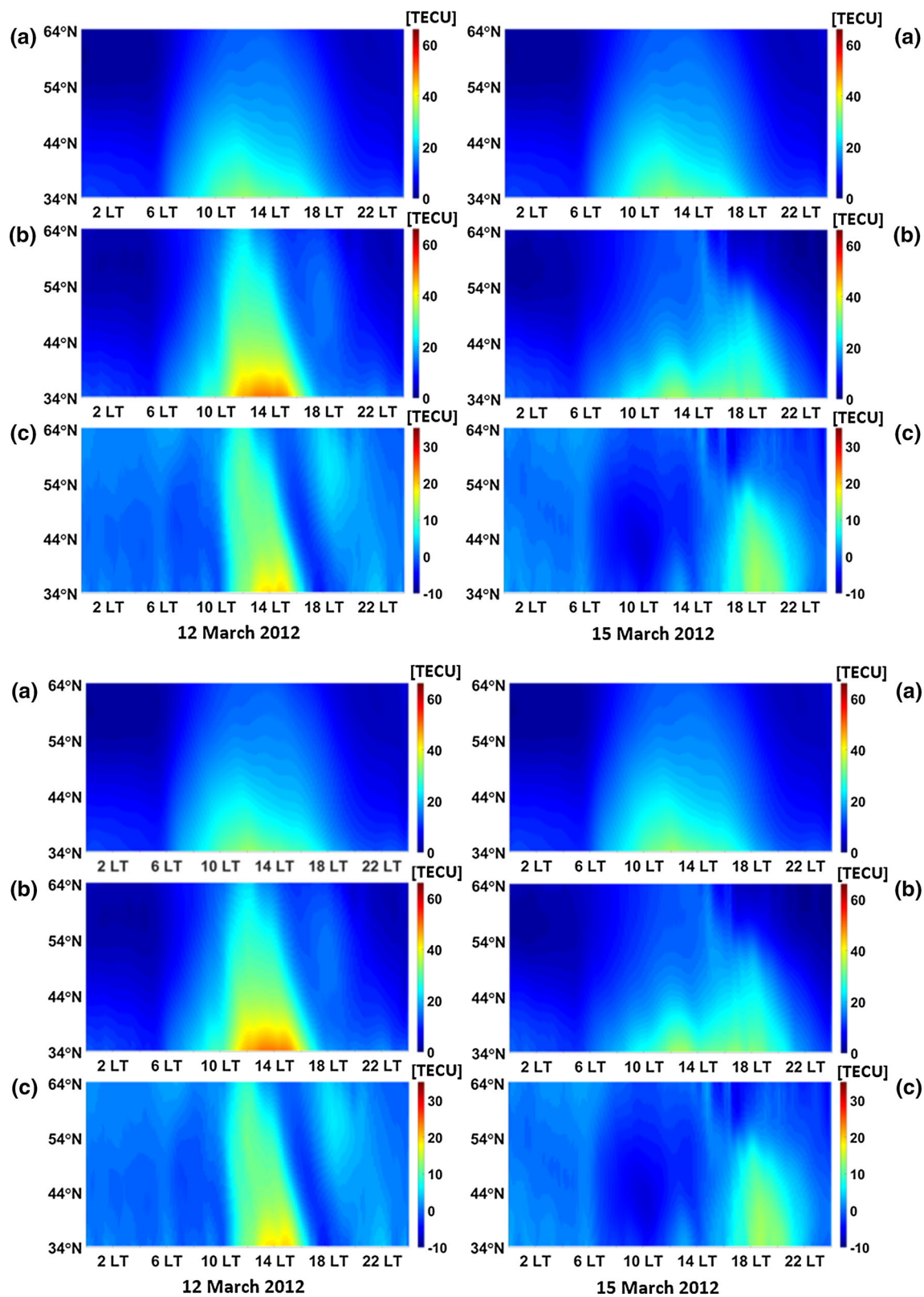


Fig. 17 Storm-time UWM-TEC deviations: **a** quiet-time background ionosphere, **b** storm-time ionosphere, **c** storm-time TEC deviation for 7, 9, 12 and 15 March 2012

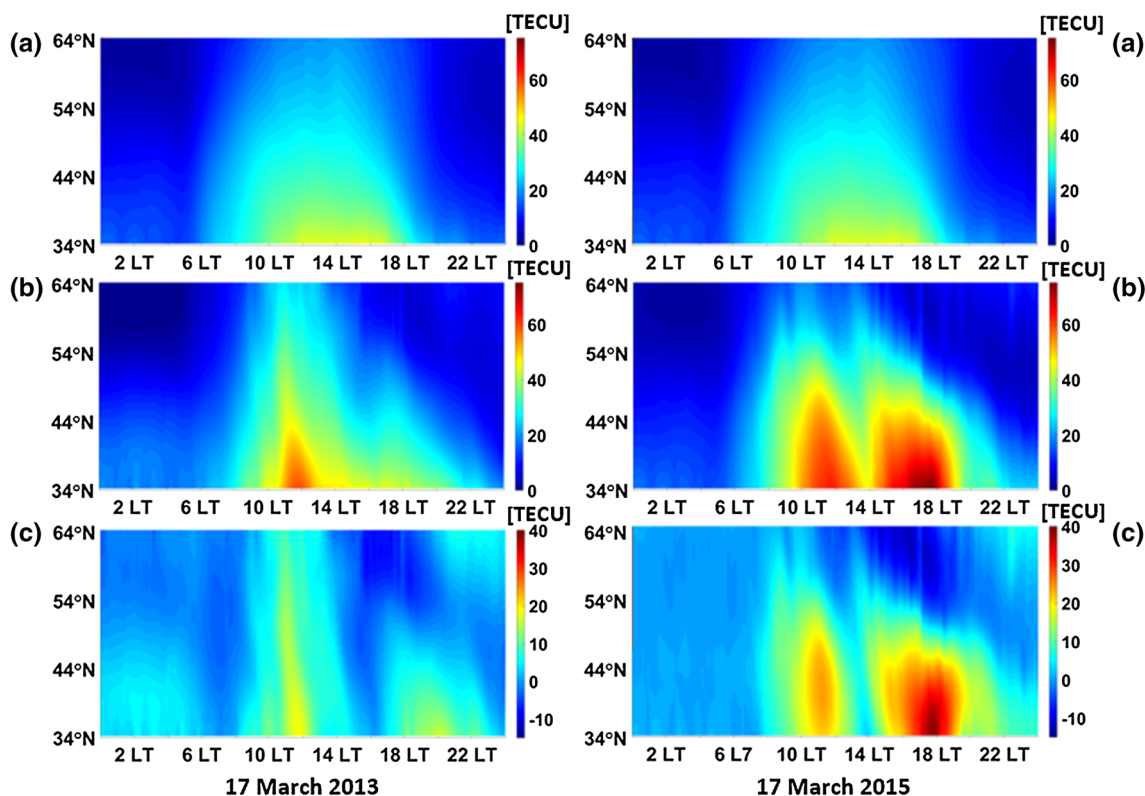


Fig. 18 Storm-time UWM-TEC deviations: **a** quiet-time background ionosphere, **b** storm-time ionosphere, **c** storm-time TEC deviation for 17 March 2013 (left) and 2015 (right)

(2016), the second TEC increase occurred during the MC passage. This second peak is observed at around 18:00 LT at the latitudes lower than 50°N. However, its maximum values reached 45 TECU and thus about 15 TECU less than during the first peak. The presented differential map in the bottom panel confirms these events. In addition, it can be seen that the increase in TEC values relative to the quiet days during the first peak amounted to 22 TECU and 13 TECU during the second peak.

In the top panel of Fig. 18, the quiet-time reference ionosphere is presented. During the background quiet period (10–16 March), TEC presented a gradual increase with its maximum reaching up 40 TECU. In the middle panel, a very clear TEC increase starting from 8:00 LT is presented. From 10:00 LT, the TEC values oscillate at the level of 60 TECU. This increase in TEC values corresponds to the sheath passage, as it has been noted by Verkhoglyadova et al. (2016). These observed TEC variations correspond to the coronal loop passage and auroral activity seen in the AE index. At about 11:00, the first TEC peak is visible, later on TEC decreases. After 14:00 LT, TEC decreases at all latitudes and then reaches its peak at 17:00 LT. A sharp drop in TEC is visible during a MC passage, and then, a pronounced negative storm signature occurred in the evening. The differential map presented in the bottom panel (Fig. 18b) allows to clearly

indicate the positive phase of the storm. In addition, two peaks of this positive effect were clearly visible in a transparent manner. It should be emphasized that the TEC increase during the second peak was twice as large with respect to the first one; moreover, this peak corresponds to the coronal loop passage and auroral activity seen in AE index.

5 Conclusions

In this paper, the dynamics of the ionosphere during geomagnetic storm periods in March 2012, 2013 and 2015 was analyzed. The strong geomagnetic storms occurred near an equinox and were driven by coronal mass ejections. The largest change in the total electron content during the stormy period of 2012 was observed on 9 March and was associated with an ICME from 7 March, which arrived on Earth 2 days later. The two events in 2013 and 2015 took place on the same day of year and were triggered by coronal mass ejections which hit the Earth at the same time of day. However, the response of the ionosphere to these two events had a completely different nature.

The impact of the space weather events during the selected periods of GNSS-TEC variations was analyzed using new regional ionosphere maps developed at UWM in Olsz-

tyn. The quality of the highly accurate and high-resolution regional ionosphere model was evaluated by a comparison to the widely used IGS GIMs. In addition, temporal TEC variations were compared with the variations of the NmF2 parameter observed by European ionosondes. This approach made it possible to assess the capability of the new high-resolution regional ionosphere model to reproduce the complex behavior of the ionosphere. The analysis of the temporal TEC changes provided by UWM maps in relation to NmF2 changes derived from ionosondes confirmed the high compatibility of these techniques for the disturbed ionosphere. In general, in all cases, UWM-TEC better reflects the changes in the disturbed ionosphere than IGS-TEC, as compared to the ionosonde data. This is also proved by the correlations between variations of NmF2 and UWM-TEC that are higher than between NmF2 and IGS-TEC during all analyzed periods.

It should be emphasized, as stated by Astafyeva et al. (2015), that widely available ionosphere maps with a time resolution of 1–2 h and low spatial resolution of several degrees may not be sufficient to analyze the storm-time effects in detail. In order to have more detailed information about the storm-time spatial and temporal TEC variations, more accurate and high-resolution ionosphere maps should be used. The presented results showed that the regional ionosphere model based on phase observations provides useful information on the response of the ionosphere to the geomagnetic disturbances. Therefore, the application of this new high-resolution model can provide more complete information about the ionosphere response to magnetic disturbances than the currently available TEC maps.

Acknowledgements The research is supported by Grant No. UMO-2013/11/B/ST10/04709 from the Polish National Center of Science.

Open Access This article is distributed under the terms of the Creative Commons Attribution 4.0 International License (<http://creativecommons.org/licenses/by/4.0/>), which permits unrestricted use, distribution, and reproduction in any medium, provided you give appropriate credit to the original author(s) and the source, provide a link to the Creative Commons license, and indicate if changes were made.

References

- Afraimovich EL, Palamartchouk KS, Perevalova NP (1998) GPS radio interferometry of travelling ionospheric disturbances. *J Atmos Terr Phys* 60:1205–1223
- Araki T, Tsunomura S, Kikuchi T (2009) Local time variation of the amplitude of geomagnetic sudden commencements (SC) and SC associated polar cap potential. *Earth Planets Space* 61:e13
- Astafyeva E, Zakharenkova I, Förster M (2015) Ionospheric response to the 2015 St. Patrick's Day storm: a global multi-instrumental overview. *J Geophys Res Space Phys* 120:9023–9037. <https://doi.org/10.1002/2015JA021629>
- Belehaki A, Cander LJ, Zolesi B, Bremer J, Juren C, Stanislawski I, Dialektis D, Hatzopoulos M (2006) Monitoring and forecasting the ionosphere over Europe: the DIAS project. *Space Weather* 4:S12002. <https://doi.org/10.1029/2006SW000270>
- Belehaki A, Tsagouri I, Kutiev I, Marinov P, Fidanova S (2012) Upgrades to the topside sounders model assisted by Digisonde (TaD) and its validation at the topside ionosphere. *J Space Weather Space Clim* 2:A20
- Belehaki A, Tsagouri I, Kutiev I, Marinov P, Zolesi B, Pietrella M, Themelis K, Elias P, Tziotziou K (2015) The European ionosonde service: nowcasting and forecasting ionospheric conditions over Europe for the ESA space situational awareness services. *J Space Weather Space Clim* 5:A25
- Belehaki A, Kutiev I, Marinov P, Tsagouri I, Koutroumbas K, Elias P (2017) Ionospheric electron density perturbations during the 7–10 March 2012 geomagnetic storm period. *Adv Space Res* 59:1041–1056. <https://doi.org/10.1016/j.asr.2016.11.031>
- Bilitza D, Reinisch BW (2008) International reference ionosphere 2007: improvements and new parameters. *Adv Space Res* 42:599–609
- Ciraolo L, Azpilicueta F, Brunini C, Meza A, Radicella SM (2007) Calibration errors on experimental slant total electron content (TEC) determined with GPS. *J Geod* 81:111–120. <https://doi.org/10.1007/s00190-006-0093-1>
- Dungey JN (1963) In: De Witt C, Hieblot J, Lebean A (eds) The interplanetary magnetic field and the auroral zones geophysics: the earth's environment. Gordon and Breach, New York, pp 526–537
- Gonzalez WD, Tsurutani BT (1987) Criteria of interplanetary parameters causing intense magnetic storms. *Planet Space Sci* 35:1101–1109
- Gonzalez WD, Joelyn JA, Kamide Y, Korchi HW, Rostoker G, Tsurutani GT, Vasyliunass VM (1994) What is a storm? *J Geophys Res* 99:5771–5792
- Hajkowicz LA (1992) Universal time effect in the occurrences of large-scale ionospheric disturbances. *Planet Space Sci* 40(8):1093–1099
- Hernandez-Pajares M, Juan JM, Sanz J (2006) Medium-scale traveling ionospheric disturbances affecting GPS measurements: spatial and temporal analysis. *J Geophys Res* 111:A07S11
- Hernandez-Pajares M, Roma-Dollase D, Krankowski A, Garcia-Rigo A, Orús-Perez R (2017) Methodology and consistency of slant and vertical assessments for ionospheric electron content models. *J Geodesy* 91(12):1–10. <https://doi.org/10.1007/s00190-017-1032-z>
- Hernández-Pajares M, Juan JM, Sanz J, Aragon-Angel A, Garcia-Rigo A, Salazar D, Escudero M (2011) The ionosphere: effects, GPS modeling and the benefits for space geodetic techniques. *J Geodesy* 85:887–907. <https://doi.org/10.1007/s00190-011-0508-5>
- Joselyn JA, Tsurutani BT (1990) A note on terminology: geomagnetic sudden impulses (SIs) and storm sudden commencements (SSCs). *EOS* 71:1808
- Klimenko MV, Klimenko VV, Ratovsky KG, Zakharenkova IE, Yasyukevich YV, Korenkova NA, Cherniak IV, Mylnikova AA (2015) Mid-latitude summer evening anomaly (MSEA) in F2 layer electron density and total electron content at solar minimum. *Space Res, Adv*. <https://doi.org/10.1016/j.asr.2015.07.019>
- Krypiak-Gregorczyk A, Wielgosz P (2018) Carrier phase bias estimation of geometry-free linear combination of GNSS signals for ionospheric TEC modeling. *GPS Solut* 22:45. <https://doi.org/10.1007/s10291-018-0711-4>
- Krypiak-Gregorczyk A, Wielgosz P, Krukowska M (2014) A new ionosphere monitoring service over the ASG-EUPOS network stations. In: 9th international conference on environmental engineering (9th ICEE) selected papers. <https://doi.org/10.3846/enviro.2014.224>
- Krypiak-Gregorczyk A, Wielgosz P, Jarmołowski W (2017a) A new TEC interpolation method based on the least squares collocation

- for high accuracy regional ionospheric maps. *Meas Sci Technol* 28(4):045801. <https://doi.org/10.1088/1361-6501/aa58ae>
- Krypiak-Gregorczyk A, Wielgosz P, Borkowski A (2017b) Ionosphere model for European region based on multi-GNSS data and TPS interpolation. *Remote Sens* 9:1221. <https://doi.org/10.3390/rs9121221>
- Liu YD, Hu H, Wang R, Yang Z, Zhu B, Liu YA, Luhmann JG, Richardson JD (2015) Plasma and magnetic field characteristics of solar coronal mass ejections in relation to geomagnetic storm intensity and variability. *Astrophys J Lett* 809:L34. <https://doi.org/10.1088/2041-8205/809/2/L34>
- Liu J, Wang W, Burns A, Yue X, Zhang S, Zhang Y, Huang C (2016) Profiles of ionospheric storm-enhanced density during the 17 March 2015 great storm. *J Geophys Res Space Phys* 121:727–744. <https://doi.org/10.1002/2015JA021832>
- Liu T, Zhang B, Yuan Y, Li M (2018) Real-time precise point positioning (RTPPP) with raw observations and its application in real-time regional ionospheric VTEC modeling. *J Geod* 1:9. <https://doi.org/10.1007/s00190-018-1118-2>
- Mannucci AJ, Tsurutani BT, Iijima BA, Komjathy A, Saito A, Gonzalez WD, Guarnieri FL, Kozyra JU, Skoug R (2005) Dayside global ionospheric response to the major interplanetary events of October 29–30, 2003 “Halloween Storms”. *Geophys Res Lett* 32:L12S02. <https://doi.org/10.1029/2004GL021467>
- Maruyama T, Ma G, Nakamura M (2009) Observations of TEC disturbances with GEONET—TEC storm and SED. *J Natl Inst Inf Commun Technol* 56:1–4
- Mendillo M (2006) Storms in the ionosphere: patterns and processes for total electron content. *Rev Geophys* 44:RG4001. <https://doi.org/10.1029/2005RG000193>
- Nie W, Xu T, Rovira-Garcia A, Zornoza JMJ, Subirana JS, González-Casado G, Chen W, Xu G (2018) Revisit the calibration errors on experimental slant total electron content (TEC) determined with GPS. *GPS Solut* 22:85. <https://doi.org/10.1007/s10291-018-0753-7>
- Okpala KC, Ogbonna ChE (2017) On the mid-latitude ionospheric storm association with intense geomagnetic storms. *Adv Space Res* 61(7):1858–1872. <https://doi.org/10.1016/j.asr.2017.08.017>
- Prolls GW (1995) Ionospheric F-region storms. *Handbook of atmospheric electrodynamics*, vol 2. CRC Press, London, pp 195–248
- Prolls GW (2006) Ionospheric F-region storms: unsolved problems, in characterising the ionosphere. In: *Meeting Proceedings RTO-MP-IST-056*, vol 10, pp 10-1–10-20. Neuilly-sur-Seine, France
- Ren X, Zhang X, Xie W, Zhang K, Yuan Y, Li X (2016) Global ionospheric modelling using multi-GNSS: BeiDou, Galileo, GLONASS and GPS. *Sci Rep* 6:33499. <https://doi.org/10.1038/srep33499>
- Schaer S (1999) Mapping and predicting the earth’s ionosphere using the global positioning system. Ph.D. Dissertation Astronomical Institute, University of Berne
- Schrijver CJ, Kauristie K, Aylward AD, Denardini CM, Gibson SE, Glover A, Gopalswamy N, Grande M, Hapgood M, Heynderickx D, Jakowski N, Kalegaev VV, Lapenta G, Linker JA, Liu S, Mandrini CH, Mann IR, Nagatsuma T T et al (2015) Understanding space weather to shield society: a global road map for 2015–2025 commissioned by COSPAR and ILWS. *Adv Space Res* 55(12):2745–2807. <https://doi.org/10.1016/j.asr.2015.03.023>
- Singh R, Sripathi S, Sreekumar S, Banola S, Emperumal K, Tiwari P, Kumar BS (2015) Low-latitude ionosphere response to super geomagnetic storm of 17/18 March 2015: results from a chain of ground-based observations over Indian sector. *J Geophys Res* 120:10864–10882. <https://doi.org/10.1002/2015JA021509>
- Tripathi R, Mishra AP (2006) Occurrence of severe geomagnetic storms and their association with solar interplanetary features. Department of Physics, A.P. University, Visakhapatnam
- Tsurutani B, Gonzalez WD, Tang F, Akasofu SI, Smith EJ (1988) Origin of interplanetary southward magnetic fields responsible for major magnetic storms near solar maximum (1978–1979). *J Geophys Res* 93(A8):8519–8531. <https://doi.org/10.1029/JA093iA08p08519>
- Tsurutani BT, Mannucci A, Iijima B, Abdu MA, Sobral JHA et al (2004) Global dayside ionospheric uplift and enhancement associated with interplanetary electric fields. *J Geophys Res* 109:A08302. <https://doi.org/10.1029/2003JA010342>
- Tsurutani BT, Echer E, Shibata K, Verkhoglyadova OP, Mannucci AJ, Gonzalez WD, Kozyra JU, Pätzold M (2014) The interplanetary causes of geomagnetic activity during the 7–17 March 2012 interval: a CAWSES II overview. *J. Space Weather Space Clim* 4:A02. <https://doi.org/10.1051/swsc/2013056>
- Verkhoglyadova OP, Tsurutani BT, Mannucci AJ, Mlynczak MG, Hunt LA, Paxton LJ, Komjathy A (2016) Solar wind driving of ionosphere-thermosphere responses in three storms near St. Patrick’s Day in 2012, 2013, and 2015. *J Geophys Res Space Phys* 121:8900–8923. <https://doi.org/10.1002/2016JA022883>
- Wu CC, Lepping RP (2011) Statistical comparison of magnetic clouds with interplanetary coronal mass ejections for solar cycle 23. *Solar Phys* 269:141–153. <https://doi.org/10.1007/s11207-010-9684-3>
- Wu CC, Lepping RP (2016) Relationships among geomagnetic storms, interplanetary shocks, magnetic clouds, and sunspot number during 1995–2012. *Sol Phys* 291:265–284. <https://doi.org/10.1007/s11207-015-0806-9>
- Wu CC, Liou K, Lepping RP, Huttung L, Plunkett S, Howard RA, Socker D (2016a) Earth: the first super geomagnetic storm of solar cycle 24: “The St. Patrick’s day event (17 March 2015)”. *Earth Planets Space* 68,151. <https://doi.org/10.1186/s40623-016-0525-y>
- Wu CC, Liou K, Vourlidas A, Plunkett S, Dryer M, Wu ST, Mewald RA (2016b) Global magnetohydrodynamic simulation of the March 15, 2013 coronal mass ejection event interpretation of the 30–80 MeV proton flux. *J Geophys Res* 121:56–76. <https://doi.org/10.1002/2015JA021051>
- Yizengaw E, Moldwin MB, Komjathy A, Mannucci AJ (2006) Unusual topside ionospheric density response to the November 2003 super-storm. *J. Geophys. Res.* 111:A02308. <https://doi.org/10.1029/2005JA011433>
- Zhang B, Teunissen PJG, Yuan Y (2017) On the short-term temporal variations of GNSS receiver differential phase biases. *J Geod* 91:563. <https://doi.org/10.1007/s00190-016-0983-9>
- Zolotukhina N, Polekh N, Kurkin V, Rogov D, Romanova E, Chelpanov M (2017) Ionospheric effects of St. Patrick’s storm over Asian Russia: 17–19 March 2015. *J Geophys Res Space Phys* 122:2484–2504. <https://doi.org/10.1002/2016JA023180>